

The Calar Alto CAFOS direct imaging first data release

M. Cortés-Contreras ¹★, E. Solano,¹ J. Alonso-Hernández,^{1,2} N. Cardiel ^{2,3}, P. Cruz ¹ and C. Rodrigo¹

¹*Centro de Astrobiología (CAB), CSIC-INTA, Camino Bajo del Castillo s/n, campus ESAC, Villanueva de la Cañada, E-28692 Madrid, Spain*

²*Departamento de Física de la Tierra y Astrofísica, Fac. CC. Físicas, Universidad Complutense de Madrid, Plaza de las Ciencias 1, E-28040 Madrid, Spain*

³*Instituto de Física de Partículas y del Cosmos, IPARCOS, Fac. CC. Físicas, Universidad Complutense de Madrid, Plaza de las Ciencias 1, E-28040 Madrid, Spain*

Accepted 2023 March 1. Received 2023 March 1; in original form 2022 April 1

ABSTRACT

We present the first release of the Calar Alto CAFOS direct imaging data, a project led by the Spanish Virtual Observatory with the goal of enhancing the use of the Calar Alto archive by the astrophysics community. Data Release 1 contains 23 903 reduced and astrometrically calibrated images taken from 2008 March to 2019 July with a median of the mean uncertainties in the astrometric calibration of 0.04 arcsec. The catalogue associated to 6132 images in the Sloan *griz* filters provides accurate astrometry and PSF calibrated photometry for 139 337 point-like detections corresponding to 21 985 different sources extracted from a selection of 2338 good-quality images. The mean internal astrometric and photometric accuracies are 0.05 arcsec and 0.04 mag, respectively. In this work we describe the approach followed to process and calibrate the images, and the construction of the associated catalogue, together with the validation quality tests carried out. Finally, we present three cases to prove the science capabilities of the catalogue: discovery and identification of asteroids, identification of potential transients, and identification of cool and ultracool dwarfs.

Key words: techniques: image processing – catalogues – virtual observatory tools.

1 INTRODUCTION

The large amount of data obtained from ground and space based telescopes make astronomical archives and catalogues prime assets for astrophysics research. They provide raw and reduced (photometrically and astrometrically corrected images, spectra ready for immediate scientific exploitation,...) data, but also high-level (catalogues, mosaics, stacked images,...) data products highly demanded by the scientific community. Projects like SDSS (York et al. 2000), 2MASS (Skrutskie et al. 2006), UKIDSS (Lawrence et al. 2007), or *WISE* (Wright et al. 2010), to name a few, are good examples of extensively used science-ready data products. Their archives are supported by a large number of refereed papers, which reflects their usefulness when conducting research projects. Archival data do also represent an advantage for the community in terms of time consumption, since they provide multiwavelength data that cover large regions of the sky without requiring new observations and their resulting processing time.

The Calar Alto Observatory (CAHA, Centro Astronómico Hispano en Andalucía) is the largest astronomical observatory located in continental Europe. Its 2.2 m telescope hosts the Calar Alto Faint Object Spectrograph (CAFOS), a versatile instrument that allows four modes of observation: direct imaging, spectroscopy, polarimetry, and narrow band imaging using a Fabry Pérot etalon. In its standard configuration, CAFOS is equipped with a 2048 × 2048 pixel blue sensitive CCD with an image scale of 0.53 arcsec pixel⁻¹.

The Virtual Observatory (VO) is a worldwide project that performs under the International Virtual Observatory Alliance.¹ Its main goal is to develop a standardized framework that enables data centres to provide competing and co-operating data services, as well as powerful analysis, visualization tools, and user interfaces to enhance the scientific exploitation of astronomical data. The Spanish Virtual Observatory (SVO²) is one of the 21 VO initiatives distributed worldwide. Among other data collections, SVO is responsible for the Calar Alto archive,³ in operation since 2011.

This paper presents the first release of the CAFOS direct imaging data, which includes reduced and astrometrically calibrated images and its associated catalogue of point-like sources. We describe in Section 2 the preparation and processing of the images. In Section 3, we present the astrometric calibration followed by the source extraction and selection, and the photometric calibration in Sections 4 and 5, respectively. The selection of images for building the catalogue is described in Section 6. The point-like catalogue of sources and validation exercises carried out with Sloan Digital Sky Survey (SDSS) DR12 (Alam et al. 2015) data are introduced in Section 7. We report two science cases carried out with the catalogue aiming at showing its potential for science exploitation in Section 8. We finish with a description on how to access the data and a summary in Sections 9 and 10, respectively.

¹www.ivoa.net

²<https://svo.cab.inta-csic.es/main/index.php>

³<http://caha.sdc.cab.inta-csic.es/calto/index.jsp>

* E-mail: mcortes@cab.inta-csic.es

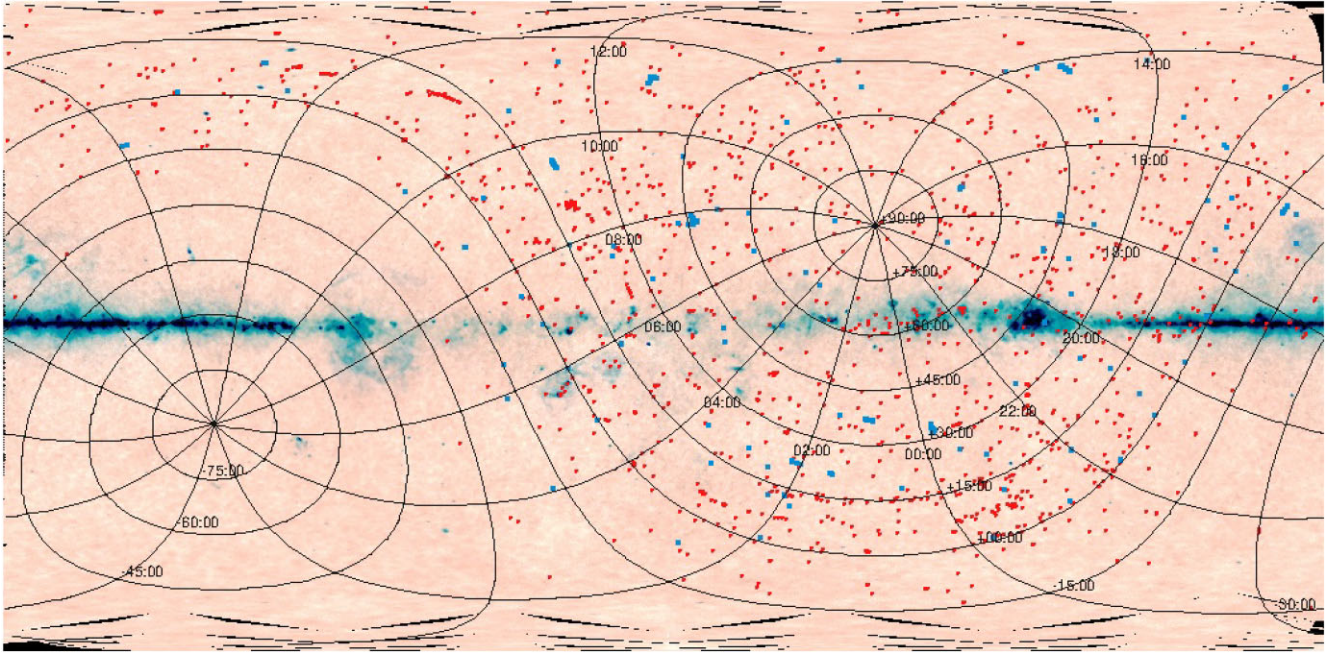


Figure 1. Location of the 42 173 (red circles) and 6616 *griz* (blue squares) CAFOS images in the sky. A Planck map is displayed in the background.

2 DATA

2.1 Data selection

The sample of images to be processed is constituted by 42 173 exposures observed with CAFOS between 2008 March and 2019 July that can be accessed from the Calar Alto archive.

For the first data release of the astrometric and photometric catalogue and to simplify, we will focus only on broad-band images observed in the Sloan system of filters *g* (λ 4750 Å), *r* (λ 6300 Å), *i* (λ 7800 Å), and *z* (λ 9250 Å). There were a total of 6616 such images observed in the Sloan’s *griz* bands between 2012 September and 2019 June, with most of them (\sim 75 percent) taken between 2017 and 2018. Another 34 607 images were observed with Johnson, Cousins, or Gunn filters, among others, that will be detailed in a later data release. There were a further 950 images with no filter information in their headers.

The location in the sky of the 42 173 and 6 616 images is shown in Fig. 1. Due to the fact that CAFOS is not a survey instrument but, quite the contrary, devoted to diverse science projects, the sky distribution of the pointings is spread all across the northern sky and covers 22.8 deg² of it (3.7 deg² in the selection of images in the Sloan’s filters).

2.2 Data processing

Each of the 42 173 images was processed using `FILABRES`,⁴ a pipeline developed at the Universidad Complutense de Madrid jointly with the Calar Alto Observatory and the Spanish Virtual Observatory (Cardiel et al. 2020). It is a software devoted to provide to the community useful images through the Calar Alto Archive. It is a three steps pipeline: (i) semi-automatic image classification into bias, flat-imaging, arc, science-imaging, etc., performed using the information of both relevant FITS keywords stored in the image

header and statistical measurements on the image data, (ii) reduction of calibration images (bias, flat-imaging) and generation of combined master calibrations as a function of the modified Julian Date, (iii) basic reduction (bias subtraction, flat fielding of the images, astrometric calibration) of individual science images, making use of the corresponding master calibrations. This software package, although designed to be run on CAFOS images, does allow the inclusion of additional observing modes and instruments.

The master calibration files are generated for each night within a given time span. In this way, science images are reduced with the master calibration files closest in time to the observations. The combination of calibration images also takes into account the signature of the images as described by the following keywords: `CCDNAME`, `NAXIS1`, `NAXIS1`, `DATESEC`, `CCDBINX`, `CCDBINY`.

All the processed images using `FILABRES` are available from the Calar Alto archive under the label *Advanced Data Products*.

3 ASTROMETRIC CALIBRATION

In this section, we describe the astrometric calibration carried out with `FILABRES` on step (iii). It is performed with the help of additional software tools provided by *Astrometry.net*⁵ and by *AstrOmatic.net*⁶ using proper motion corrected *Gaia* DR2 data (Gaia Collaboration 2016, 2018). *Astrometry.net* provides an initial astrometric calibration refined afterwards with the *AstrOmatic.net* software, which includes the use of `SCAMP` (Bertin 2006).

Of the 42 173 images in the Calar Alto archive, 18 270 have no astrometric reduction at all, 1050 do only have the initial astrometric calibration performed with *Astrometry.net* tool and 22 853 images have the additional *AstrOmatic.net* solution as well. Therefore, 57 percent (1 050 + 22 853) of the images in the archive present an astrometric calibration.

⁴<https://filabres.readthedocs.io/en/latest/>

⁵<http://astrometry.net/doc/readme.html>

⁶<https://www.astromatic.net/>

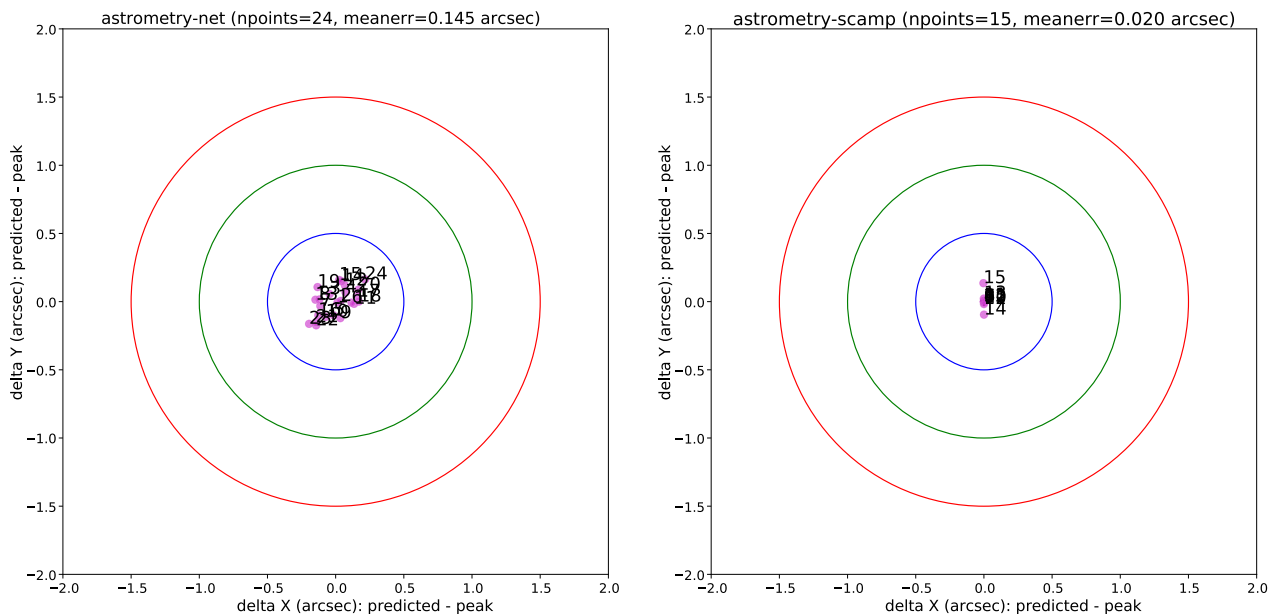


Figure 2. Differences between the predicted location of the sources and the peak positions using the astrometric solution found with *Astrometry.net* (left-hand panel) and *Astrometry.net* + *AstrOmatic.net* (right-hand panel) softwares. Each source is labelled with a number.

The median of the mean errors in the initial astrometric calibration with the *Astrometry.net* tools in the 22 853 images for which both astrometric solutions were computed is 0.38 arcsec. This value downs to 0.04 arcsec after running the *AstrOmatic.net* software.

Regarding the sample of 6616 images observed in the Sloan bands, 6132 present both astrometric solutions, with median values of the mean errors of 0.18 arcsec after the initial calibration and 0.03 arcsec after the second one. Fig. 2 compares the differences between the predicted location of the sources and the peak positions found in the images with the *Astrometry.net* and *AstrOmatic.net* astrometric solutions.

4 SOURCES

4.1 Source extraction

We developed the CAFOS Photometry Calibrator⁷ (CFC), a pipeline designed for (i) measuring the instrumental photometry of sources in CAFOS images, (ii) performing a selection of these sources using different filtering criteria and (iii) carrying out the photometric calibration. CFC can be run directly over the `FILABRES` structure of folders to use as an input the astrometrically calibrated images provided by the software. It can be run as well over independently reduced and astrometrically calibrated images. In both cases, it is possible to include an additional csv configuration file containing the CAHA numerical identifier, the filter of observation, the name of the file, or the path to the images. If the filter field is empty or the pipeline does not identify it, it proceeds to look for it in the image header. By default, it only processes images observed in the Sloan *griz* bands. All other images will be reported in a log file.

CFC performs a step by step process to identify the image sources and estimate their instrumental parameters using `SEXTRACTOR` (Bertin & Arnouts 1996) and `PSFEX` (Bertin 2013). The method is based on a first iteration of `SEXTRACTOR`, whose output catalogue

is used by `PSFEX` to estimate the PSF model of the image sources. The PSF model is then used in a second iteration of `SEXTRACTOR` to fit every source using standard PSF fitting.

We kept sources above 1.5σ of the local background and with less than 50 000 counts as an approximate value for saturation. Remaining saturated sources will be removed as described in Section 5, since they are subject to larger uncertainties in their astrometry and photometry.

We measured `MAG_PSF` photometry, suitable for point-like detections, and we extracted some morphometric parameters like the full-width at half-maximum (FWHM), the flux radius (defined as the circular aperture radius enclosing half the total flux), the signal-to-noise ratio, the elongation, and the ellipticity. We also included the `SPREAD_MODEL` parameter, a star/galaxy estimator based on model fitting. This parameter will be useful for creating our point-like catalogue. Besides, we add the minimum and maximum x and y coordinates among detected pixels (`XMIN_IMAGE`, `XMAX_IMAGE`, `YMIN_IMAGE`, `YMAX_IMAGE`).

The `SEXTRACTOR` and `PSFEX` configuration files used to produce the catalogues of sources are given in Tables A1 and A2, and the first output of the pipeline would be the `SEXTRACTOR` catalogues with the columns listed in Table A3.

4.2 Source selection

Aiming at removing spurious detections from the catalogue, we discarded sources with `FLUX_MAX`, `FLUX_RADIUS`, `FWHM_IMAGE`, and `FLUX_PSF` smaller than or equal to zero, `MAG_PSF` and `MAGERR_PSF` equal to 99 (meaning that `SEXTRACTOR` PSF fit did not converge), `MAGERR_PSF` equal to zero or larger than 1 mag, and `FLAGS_WEIGHT` (weighted extraction flag related to the presence of close neighbours bright enough to significantly bias the photometry, bad pixels, blended objects, saturated pixels, or other features) equal to two. We also neglected sources with `SNR_WIN` smaller than five or equal to $1e30$, which has no physical meaning. The limit in `SNR_WIN` at five is set to avoid sources with very poor photometry, while the latter is related to a bad extraction of the source.

⁷<https://cafes-photometry-calibrator.readthedocs.io/en/latest/>

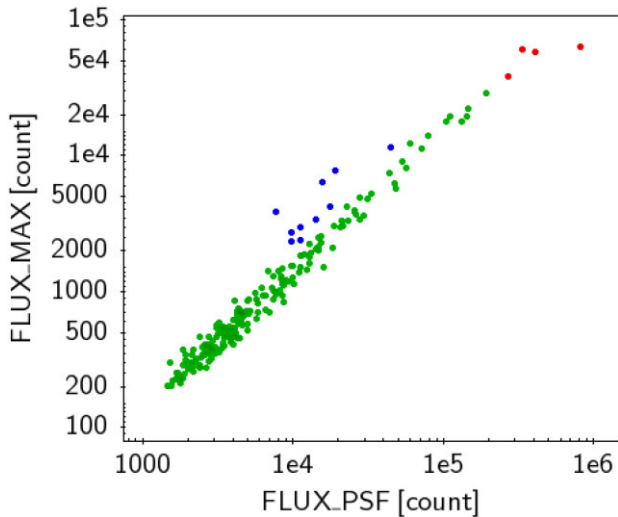


Figure 3. Flux at the peak (FLUX_MAX) versus integrated flux (FLUX_PSF) in logarithmic scale for detections in one image. Spurious, saturated, and valid detections are represented in blue, red, and green, respectively.

As mentioned before, we set a saturation level when extracting sources in our images at 50 000 counts. However, some saturated detections could remain unidentified. We attempt to remove them together with the resting spurious detections such as bad pixels, cosmic rays, and artefacts with a complementary procedure similar to that followed in Cortés-Contreras et al. (2020). It accounts for the linear relation between the flux at the peak of the distribution (FLUX_MAX) and the integrated flux (FLUX_PSF), as shown in Fig. 3. It is a two steps procedure that can summarized as follows: In a first place and in order to discard spurious detections in each image, we kept detections which $\text{FLUX_MAX}/\text{FLUX_PSF}$ ratio deviates by less than 2σ from the mean value. We recomputed the mean and standard deviation of the flux ratio of the remaining set of sources and kept detections with ratios under the mean value plus 3σ . Afterwards and aiming at identifying saturated sources, we look for the value of FLUX_PSF in each image at which linearity breaks due to saturation with two simultaneous approaches (i) when the slope of the curve FLUX_MAX versus FLUX_PSF varies by more than 1 per cent, or (ii) when the Pearson correlation coefficient r of the linear fit is lower than 0.98. Both of them are evaluated increasing the number of points towards increasing values of FLUX_PSF . The approach that provides the lowest FLUX_MAX is applied. We then compute the standard deviation of the sample of sources that present fluxes above that cut value and remove from the catalogue all sources with FLUX_MAX greater than the cut value minus 1σ .

5 FLUX CALIBRATION

We chose the SDSS DR12 (Alam et al. 2015) and APASS DR9 (Henden et al. 2015) surveys as the photometric references to calibrate our catalogue. For this, the first step is to make the selection of calibration sources. To select them, we first cross-matched the SExtractor catalogue of detections of each individual image with SDSS DR12 within 2.0 arcsec. We kept all counterparts in that radius and then applied the following criteria to define the calibration sources:

(i) SDSS sources must be point-like ($\text{class} = 6$) and flagged with $\text{q_mode} = '+'$ and $\text{mode} = 1$, indicating clean photometry of primary detections.

(ii) SDSS sources must be within the detection and saturation limits⁸

(iii) Both SExtractor and SDSS magnitude uncertainties must be smaller than 0.2 mag.

(iv) FWHM, elongation, and ellipticity values must be within the median values of the image and twice the interquartile. This serves to morphometrically identify spikes and extended sources and remove them from our CAFOS catalogue.

For each image, we kept the sources fulfilling the conditions given above and carried out a sigma-clipping linear fit between the CAFOS SExtractor and SDSS DR12 calibrated magnitudes.

We performed the photometric calibration only in images with at least six calibrating point-like sources and when the Pearson correlation coefficient (r) of the fit is greater than 0.98. When the sky region was not covered by SDSS DR12 observations or the number of calibration sources was lower than six, we performed the calibration with the APASS DR9 photometric catalogue applying the two latest criteria described above and selecting only APASS counterparts with magnitudes in the range $7 < V < 17$ magnitudes. We calibrated 3964 images (out of 6616), 3334 of which were calibrated with SDSS DR12 and 630 with APASS DR9 photometry. A column indicating the reference catalogue used for the calibration (SDSS or APASS) is included in the final catalogue. Moreover, since the range of magnitudes reached in each image may be larger than the range of magnitudes of the calibration stars, we also include in the final catalogue a calibration flag that indicates whether the calibrated magnitudes are within the interval of magnitudes used for the photometric calibration (A), fainter (B), or brighter (C). The 71 per cent of the calibrated magnitudes lies within the interval of magnitudes used for the photometric calibration, only 4 per cent present fainter magnitudes and 25 per cent show brighter magnitudes than those used for the calibration.

The calibration residuals of CAFOS magnitudes as a function of the reference magnitudes are shown in Figs 4 and 5, together with the distributions of the absolute values of the magnitude differences. In the first and third panels, we show the average magnitude differences in bins of 0.5 mag with more than ten points. In the calibration with SDSS, the average magnitude differences increase at fainter magnitudes (21.5 mag in the filters g and i , 22.0 mag in r and 17.0 mag in z). The i band presents a large magnitude difference at 15 mag. A detailed inspection of these detections reveals that the good-quality ($\text{q_mode} = '+'$ and $\text{mode} = 1$) SDSS magnitudes are around 0.5 mag fainter than the secondary measurements ($\text{mode} = 2$), which agree better with our photometry, yielding a mean difference of 0.14 mag instead of -0.41 mag. With that exception, the averaged differences of magnitudes remain under 0.17 mag in all bands. For the calibration done with APASS, we observe that in the g and i bands the average magnitude difference increases at the edge of the plot at 17 mag and 15.5 mag, respectively. In this case, the averaged differences of magnitudes remain under 0.05 mag in all bands. Mean magnitude absolute differences (second and fourth panels) vary from 0.06 to 0.12 mag for the comparison with SDSS data and from 0.04 to 0.07 mag in for APASS', depending on the filter.

We show the normalized cumulative distributions of the magnitude differences with SDSS DR12 and APASS DR9 in top and bottom panels of Fig. 6, respectively. The photometric scatter in absolute values in 90 per cent of the sample is under 0.27/0.09, 0.21/0.16, 0.18/0.12, and 0.14 magnitudes in g , r , i , and z bands, respectively, compared to SDSS/APASS.

⁸For details, see https://www.sdss.org/dr16/imaging/other_info/

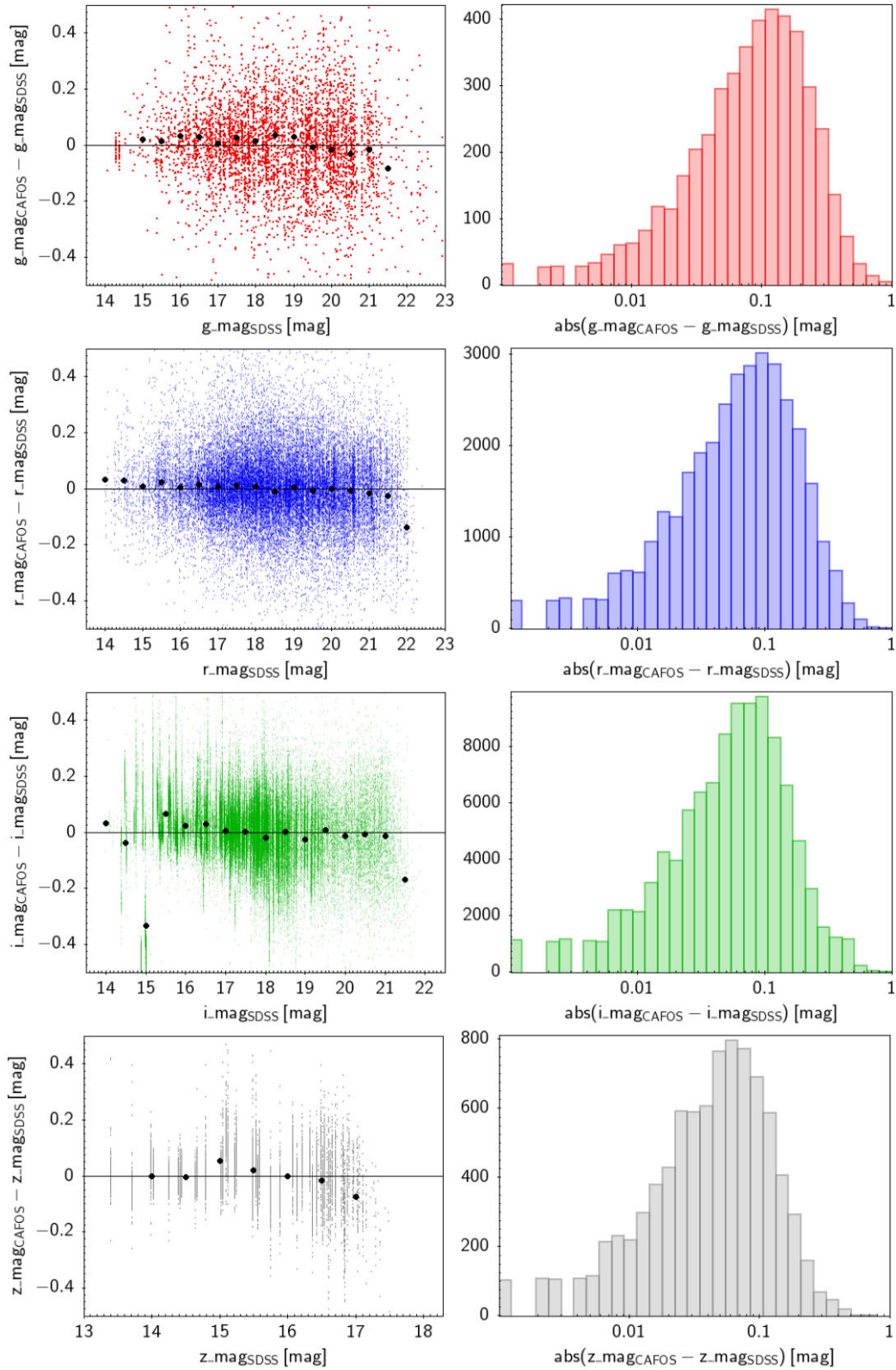


Figure 4. Comparison between SDSS DR12 and CAFOS magnitudes of the sources used for the photometric calibration. On the left-hand panels, black filled circles represent the average difference of magnitudes in bins of 0.5 mag. Only bins with ten or more sources are represented. Right-hand panels represent the distributions of the absolute values of the magnitude differences.

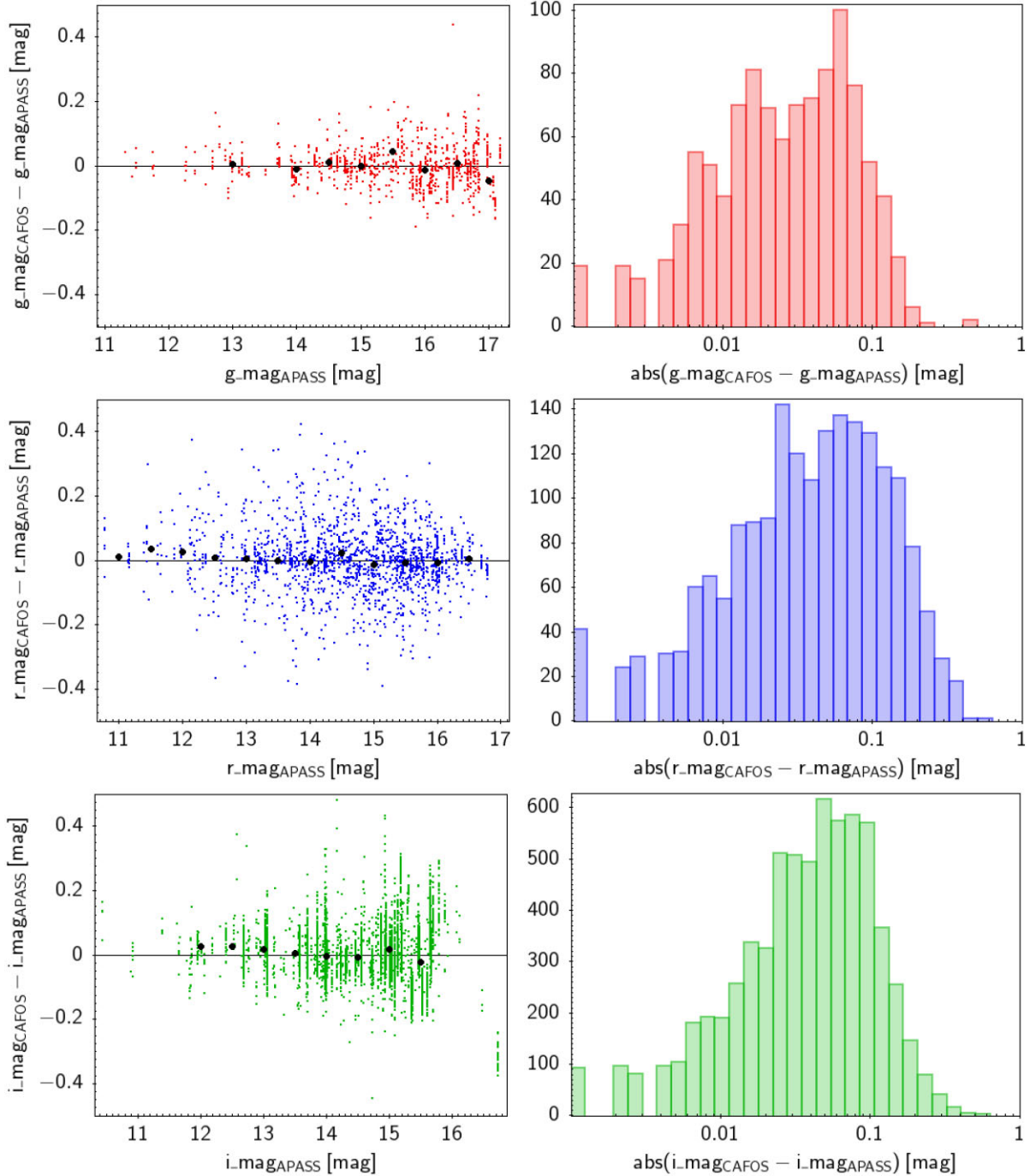


Figure 5. Comparison between APASS DR9 and CAFOS magnitudes of the sources used for the photometric calibration. On the left-hand panels, black filled circles represent the average difference of magnitudes in bins of 0.5 mag. Only bins with ten or more sources are represented. Right-hand panels represent the distributions of the absolute values of the magnitude differences.

6 IMAGE SELECTION

Among the 3964 photometrically calibrated images, there are 85 images with no astrometric calibration carried out by *AstrOmatic.net* but only by *Astrometry.net*. We compared the coordinates of the detections in these images to the astrometry from *Gaia* EDR3 and obtained a mean difference of near 1 arcsec between coordinates. We considered this value too high to be included in our catalogue and, therefore, these images were discarded.

Also, it is not uncommon to find in our data set of images observed with CAFOS blurred images or images out of focus due to bad weather conditions, wrong settings, or defocused on purpose.

The image quality has a measurable impact on the *SEXTRACTOR* FWHM and the absolute differences between the object position and the windowed position estimate along the x and y axes $|X_IMAGE - XWIN_IMAGE|$ and $|Y_IMAGE - YWIN_IMAGE|$ of the detections. The former is a reflection of the dispersion produced by the telescope and the atmosphere in the photons received from a

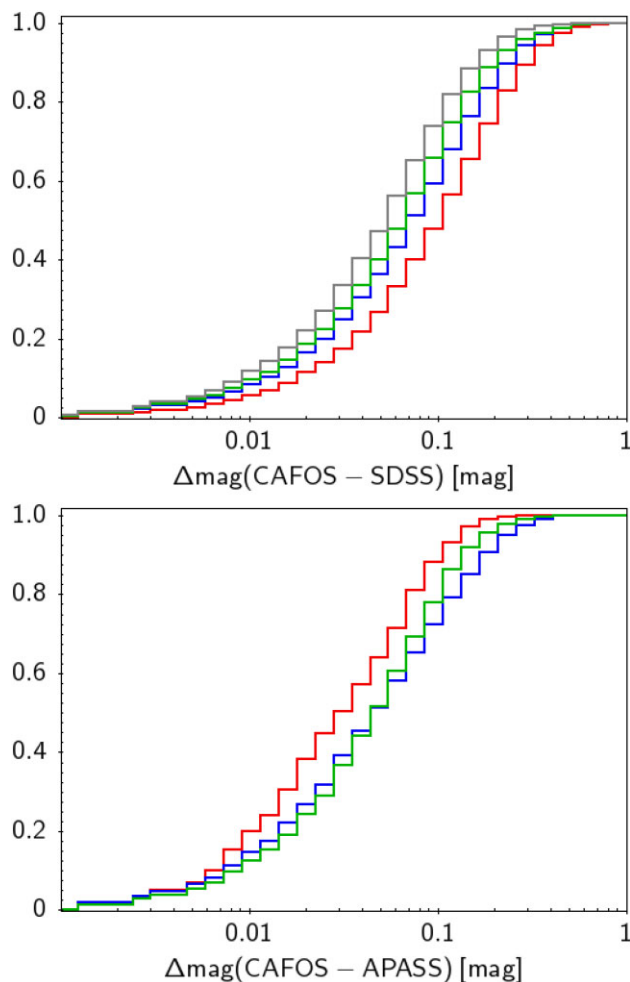


Figure 6. Normalized cumulative distribution of absolute magnitude differences between CAFOS and SDSS DR12 (top) or APASS DR9 (down) in logarithmic scale in the g (red), r (blue), i (green), and z (grey) bands.

point source over several pixels in the CCD. The latter is related to the centroiding accuracy of `X_IMAGE` and `Y_IMAGE`, which should be very close to that of PSF fitting as stated in the documentation of `SEXTRACTOR`. Hence, abnormal values (lower or higher than a typical value, as described below) would be associated to low quality images taken under bad weather conditions or with a large fraction of saturated or extended sources. We therefore used them to assess the quality of an image, together with the mean error of the astrometric calibration provided by `FILABRES`.

As a first step, we removed from the catalogue all detections with `FWHM` and `Elongation` that deviate by more than 2σ from the median value of each image. We then identified from visual inspection a sample of 404 good-quality images taken in 2017. These images were used to obtain reference values of the `FWHM`, `|X_IMAGE-XWIN_IMAGE|`, and `|Y_IMAGE-YWIN_IMAGE|`. For each image, we obtain the median of each of them. With the set of values of the 404 images, we got three upper limits defined as the median values plus 3σ for the `FWHM`, `|X_IMAGE-XWIN_IMAGE|`, and `|Y_IMAGE-YWIN_IMAGE|`: 3.96 arcsec, 0.10 pix, 0.13 pix, respectively. We observed that the mean internal uncertainties from `FILABRES` take values under 0.09 arcsec in this set of images. We kept this value as the upper limit for selecting useful images among the photometrically calibrated images.

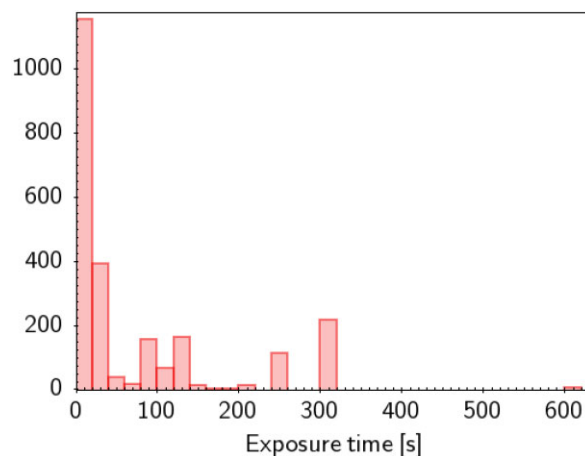


Figure 7. Distribution of the exposure times of the 2338 images selected for the catalogue.

For each of the remaining 3475 calibrated images (3964–85–404), we computed the median of the `FWHM`, `|X_IMAGE-XWIN_IMAGE|`, and `|Y_IMAGE-YWIN_IMAGE|`. Together with the astrometric error from `FILABRES`, we rejected images which median values are greater than the upper limits defined above. We ended up with 2338 images from over 55 different nights taken between 2012 September and 2019 June. This set contains 218 782 detections.

By visual inspection, we found that some slightly defocused images still remain. We estimated the fraction of these images to be no larger than 10 per cent. Nevertheless, the comparison between our calibrated photometry and Sloan’s shows differences under 0.1 mag in average, which is in accordance with what we have presented in Section 5.

The exposure time distribution of the selected images is shown in Fig. 7. In the whole catalogue, exposure time ranges from 0.5 to 600 s, although in the z band the interval varies from 2.5 to 20 s. As an average, selected images in all filters have an exposure time of 69 s and the median of the distribution lies at 20 s. For very short exposure times, the effect of atmospheric turbulence may be imperfectly time-averaged, meaning the PSF used for extracting fluxes could differ from a smooth Moffat-like function and could also vary over the field of view. We observe that a large fraction of the dropped images (85 per cent) have exposure times under 40 s (10 s as a median), which agrees with the before mentioned effects noticeable at short integration times. In addition, we also assessed their impact on the astrometric residuals and found no particular trend either on kept or rejected images.

7 A POINT-LIKE SOURCE CATALOGUE

For the first data release, our main purpose is to provide a point-like photometric catalogue from the CAFOS images with SDSS filters available at the CAHA archive, i.e. a collection of images taken for different science cases and therefore, showing different observational parameters. The choice of a point-like catalogue alone in this first data release is made by simplicity and motivated by the shallower depth compared for instance to the GTC Osiris DRI catalogue previously published by this group following a similar procedure (Cortés-Contreras et al. 2020).

After the cleaning in `FWHM` and elongation described in Section 6, we used the `SPREAD_MODEL` parameter to identify point-like sources. This parameter shows values close to zero for point sources,

Table 1. Number of detections per filter in the catalogue.

Filter	Number of images	Number of detections
Sloan <i>g</i>	169	8695
Sloan <i>r</i>	529	52 244
Sloan <i>i</i>	1184	69 759
Sloan <i>z</i>	456	8637

positive for extended sources (galaxies), and negative for detections smaller than the PSF, such as cosmic ray hits. To define the value of the `SPREAD_MODEL` that separates point sources from extended sources and cosmic rays, we made use of the object type provided by the SIMBAD astronomical data base (Wenger et al. 2000). There are 9568 detections in our clean catalogue with a SIMBAD entry within 2 arcsec. Of them, 5795 are classified as ‘stars’ and 1415 as ‘galaxies’ (we excluded any other classification). We observed two close peaks in the distributions of the `SPREAD_MODEL` of these two sets with mean values of 0.008 ± 0.024 (stars) and 0.022 ± 0.018 (galaxies). The fraction of detections in the negative wings of the distributions is negligible. After different tests, we defined a detection as point-like if its associated `SPREAD_MODEL` lies in the interval $[-0.011, 0.013]$. This minimizes the contamination of galaxies in the sample and, at the same time, maximizes the completeness of stars. Detections with values below or above that range will be considered as artefacts and extended, respectively, and will be removed from the catalogue.

To assess the goodness of this approach, we compared our classification with the object type provided by SDSS DR12 under the *class* column. The completeness of point-like sources reached 89 per cent, while the contamination is of 15 per cent in this interval.

We set up different limits in the FWHM and ellipticity, and refine the lower limit of the `SPREAD_MODEL`, aiming at removing detections that present anomalous values probably related to a wrong extraction of the sources but also to contamination in the catalogue. We established an upper limit in the FWHM at 3.9 arcsec from the median and three times the MAD (median absolute deviation) values of the whole catalogue of point-like sources. The FWHM lower limit is naturally set by the first centile at 0.8 arcsec. From the resulting catalogue with FWHM between 0.8 and 3.9 arcsec, we eliminate sources with `SPREAD_MODEL` < -0.008 and ellipticities larger than 0.4, corresponding to the first and 99th centiles, respectively. As a result, the catalogue contains 139 337 point-like detections from 2338 images distributed over 54 different nights.

Detections were grouped into sources by carrying out with STILTS (Taylor 2006) an internal match of the whole catalogue (this is, regardless the photometric band) within 0.5 arcsec. This value is a good compromise between completeness and reliability. Larger values may produce associations among unrelated detections. Smaller values could miss faint detections, which typically show large centroiding errors or sources with high proper motions. This way, the 139 337 detections were grouped in 21 985 different sources, each of which presents a numerical identifier in the catalogue. Note that the absence of a source in the catalogue does not imply that it has not been detected by CAFOS but that it might not have passed the quality tests. We thus address him/her to the Calar Alto archive to obtain its photometry from the ready-to-use science images.

Table 1 lists, for each filter, the number of images and detections contained in the catalogue while Table 2 summarizes the number of sources that have been detected in one, two, three, or the four bands, regardless which bands they are. Almost 84 per cent of the sources in the catalogue have been detected in just one band and none has been

Table 2. Number of sources detected in one to four bands.

Number of bands	Number of sources
4	0 (0 per cent)
3	1 250 (5.7 per cent)
2	2 356 (10.7 per cent)
1	18 379 (83.6 per cent)

detected in the four bands. A detailed description of each column in our detection catalogue is given in Table B1.

The mean internal astrometric accuracy in the catalogue is 0.05 arcsec computed as the quadratic sum of the uncertainties in right ascension and declination as obtained from the `SEXTRACTOR` parameters `ERRX2_WORLD` and `ERRY2_WORLD`. The comparison with *Gaia* EDR3 within 2 arcsec after correcting for proper motions provides a median position distance of 0.08 ± 0.04 arcsec, which we consider to be a more realistic assessment of the astrometric accuracy of the catalogue.

The magnitude coverage in the catalogue from the faint to the bright end ranges between 10.6 and 20.6 mag in *g*, 10.7–21.0 mag in *r*, 10.8–20.7 mag in *i*, and 9.4–16.6 mag in *z*. For each filter, the brightest magnitude corresponds to the minimum value of the magnitudes in the catalogue. The magnitudes at the faint edge are set by the 90th percentile. The magnitude limits in the CAFOS catalogue are between 1.3 and 2.5 magnitudes brighter than SDSS’s in the *gri* bands, and 4.1 mag brighter in the *z* band. The large difference in the *z* filter is explained by the exposure times of the images. While in the *gri* filters exposure times are between 55 and 136 s as an average, the average exposure time in the *z* filter is 6 s.

To illustrate the sensitivity reached in the catalogue in the four filters, we represent in Fig. 8 the estimated photometric uncertainties averaged in bins of 0.5 mag, as a function of magnitude. Magnitude uncertainties increase towards fainter magnitudes. Mean magnitude uncertainties are entirely under 0.16 mag in all bands and the mean internal photometric accuracy of the catalogue is 0.04 mag. The comparison with SDSS photometry presented in Section 5 yields a more realistic averaged accuracy of 0.09 mag.

7.1 Catalogue quality assessment

7.1.1 Internal photometric precision

The comparison of the magnitude of sources observed more than five times in the same filter allows us to estimate the internal photometric precision of the catalogue. We show in Fig. 9 the relation between their standard deviations and magnitudes. The averaged photometric errors of Fig. 8 are also represented in the above mentioned figure.

The dispersion in the standard deviation of magnitudes increases towards fainter magnitudes in the *gri* bands. In the *r* filter this variation looks flatter and also presents large standard deviations. In the *z* filter the scatter at bright magnitudes decreases up to 13.5 mag, where it increases again. The variation of magnitudes of repeated sources is overall over the averaged photometric errors from Fig. 8. The largest differences in *g* in the range between 16 and 21 mag are partially within the defined error bars, and in *r* the differences are almost entirely within the error bars. The *i* band photometry is in good agreement with the mean accuracy of the catalogue. In *z* band, the discrepancy between magnitude variations and the averaged photometric errors is large at bright magnitudes and up to 13.5 mag, from where it behaves accordingly. There seems to be no relation between

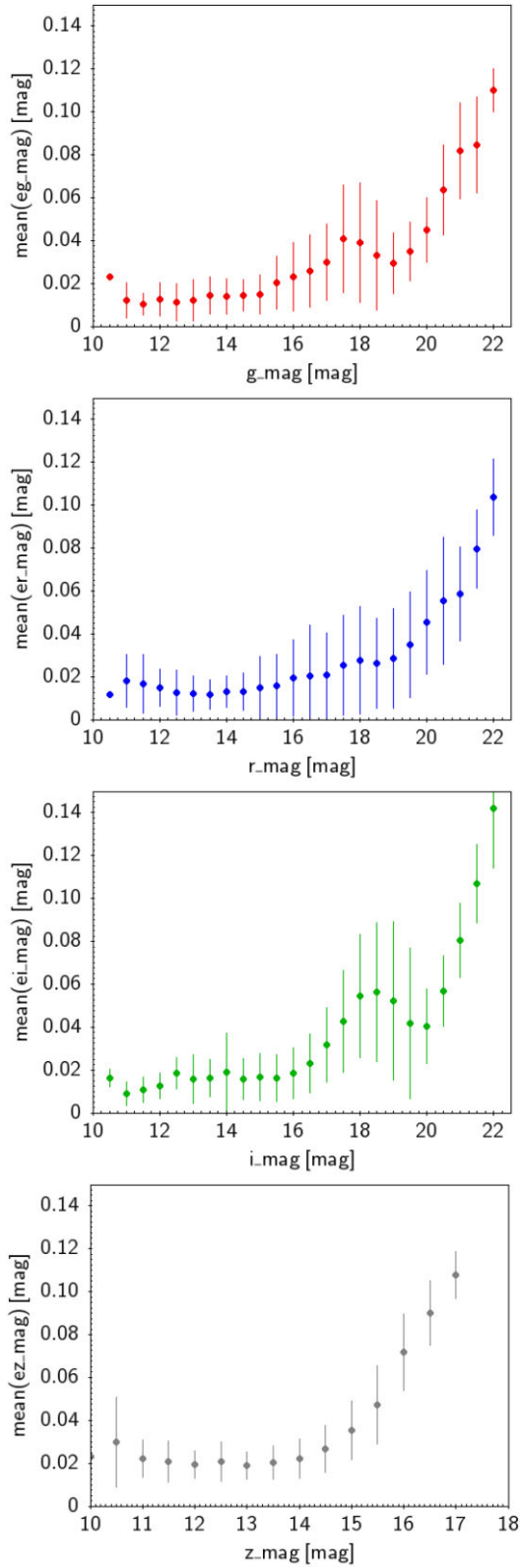


Figure 8. Internal photometric errors versus magnitudes in the four bands. Bullets are the average values of the magnitude uncertainties in bin sizes of 0.5 mag and the error bars show the standard deviation.

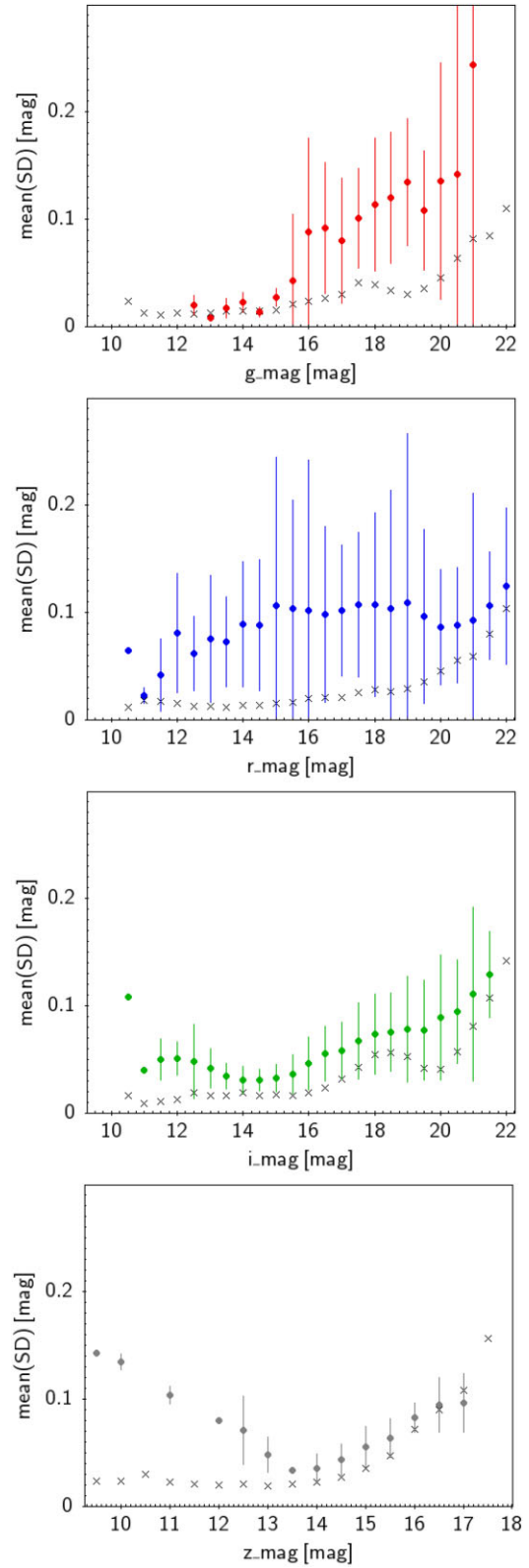


Figure 9. Photometric repeatability as a function of magnitudes for sources observed more than five times. Bullets are the averaged values of the standard deviations of magnitudes of repeated sources in bin sizes of 0.5 mag and the error bars show their standard deviation. Mean values of the average photometric errors shown in Fig. 8 are displayed as black crosses.

the observed differences in the g and r bands and the exposure times of the images or the number of sources used for the statistics that could explain the larger deviations noted in these bands compared to i and z . Revisiting the calibration parameters does not reveal any inconsistency among filters and neither preferred sky positions nor particular epoch of the year of the observations. Other factors that are not taken into account and could affect the photometry could be related to the weather conditions and phase and location of the Moon, for instance. We recall that our sample of data has not been obtained under a systematic configuration but under a diversity of observing configurations adjusted to the different scientific purposes. Among them are variability studies (i.e. transits, stellar spots, pulsations...). The presence of variables in the catalogue is addressed in Section 7.1.3.

Despite those apparently larger dispersions in the bluer filters, the averaged standard deviation of sources detected more than five times in each filter is of 0.08 mag. It is quite consistent with the averaged magnitude differences between CAFOS and SDSS photometry of 0.09 mag obtained in Section 5.

7.1.2 Colour, binning mode, and pixel position dependence

The comparison of the colour differences between CAFOS and SDSS or APASS as a function of the calibrated magnitudes allows us to assess the effect of a colour term in the photometric calibration. As expected, since our images have been observed with the same set of filters used by SDSS or APASS, there is no colour effect.

We also verify whether there exists a relation of the observed magnitude differences with the pixel position of the sources in the CCD. We show in Fig. 10 the xy windowed pixel positions from SEXTRACTOR of good-quality sources in SDSS DR12 and APASS DR9 that display absolute differences over the mean values in each filter presented in Section 5 (0.27/0.09, 0.21/0.16, 0.18/0.12, and 0.14 magnitudes in g , r , i , and z in SDSS/APASS, respectively). The different observing modes of CAFOS are clearly seen. We observe some overdensities in the r band in images where SDSS is the reference catalogue for photometric calibration at different positions of the CCD. For example, those located around the pixel positions (100,275), (230,50), (420,530) are clearly identified and correspond to over 170 detections of the same source. A similar behaviour is observed in the i band in images where APASS is the reference catalogue for photometric calibration at (260,310), (300,220), or (730,20), for instance, with more than 35 detections of the same target. Hence, these clumps could not be ascribed to a pixel position dependence but to different measurements of the same object over the same observing run.

In general, the random configuration of the sources in the CCD reflects that the magnitude differences do not depend on the binning mode of observation nor the pixel position.

7.1.3 Variability

Over 54 nights, the catalogue maps 89 different sky regions, some of which have been intensively surveyed.

To assess whether the observed differences between magnitudes of repeated objects and the mean accuracy of the catalogue are associated to real variable sources, we analyse the magnitude variations according to the following equation:

$$S = \text{mag}_{\min} + 5 \cdot e_{\text{mag}_{\min}} - (\text{mag}_{\max} - 5 \cdot e_{\text{mag}_{\max}}), \quad (1)$$

where mag_{\min} , mag_{\max} , $e_{\text{mag}_{\min}}$, and $e_{\text{mag}_{\max}}$ are the lower and higher magnitudes measured for the same source and their associated errors. We chose 5σ to take into account for the underestimated photometric uncertainties in the catalogue.

We cross-matched the whole catalogue with the AAVSO International Variable Star Index VSX (Watson et al. 2006) and obtained 51 different sources that have been observed with CAFOS in at least one filter. We kept the 21 sources observed five or more times in the same filter in our catalogue and obtained an average value of $S = -0.038 \pm 0.082$ mag for variable objects. A negative value of S means that the magnitude deviation of the source is outside the reach of five times the errorbars and cannot be explained by photometric errors. Aiming at minimizing the contamination of sources that could present large scatter in magnitudes due to the different observing conditions, we set S at -0.12 mag (median -1σ) and looked for variable candidates in our catalogue that fulfill $S < -0.12$ mag.

Between 8 and 33 percent of the sources that have been detected at least five times in the same filter have associated a value of $S < -0.12$ mag, depending on the filter. We show the normalized distribution of magnitudes of these sources in the four filters in Fig. 11. As a reference, we display in each filter the magnitude detection limits as defined in Section 7. The peaks of the distributions are well below these limiting magnitudes. We conclude that the magnitude variations cannot be entirely ascribed to faint sources which could present lower quality photometry. In Fig. 12 we compare the ellipticity, FWHM, and `spread_model` of detections with S over and below -0.12 mag. The distribution of ellipticities, FWHM, and `spread_model` are similar in detections with $S < -0.12$ mag (suspected variables) and with $S \geq -0.12$ mag. This means that potential biases in the morphometric parameters <https://www.overleaf.com/project/60d5cdc54d3e31d7eb91088e> are responsible for the observed variability.

On the other hand, we compared the standard deviation of magnitudes of the 21 sources with counterparts in the VSX catalogue with at least five measurements in the same band, with respect to their mean magnitudes in the corresponding filter (Fig. 13). We identify nine sources with a standard deviation equal to or larger than the difference between the maximum and the minimum magnitudes (or the amplitude), as provided in VSX. Each of them are labelled from 1 to 9 in Fig. 13.

Source #1 (CRTS J074523.2+460549) is a known eclipsing binary that presents the largest variation in the r band ($SD = 0.4$ mag). Sources #2 (NSV 25135) and #3 (ZTF J065139.43-002656.9) also show relatively large variations in the r band. The former is catalogued in VSX as a suspected variable that lacks deeper study and the latter is defined as a BY Draconis-type. The variation in amplitude estimated from the CAFOS images (0.15 mag) is in agreement with what is expected from these flaring stars. Also, the chromospheric activity associated to this class of objects could explain the large variations seen in the r band. Sources #4 (WASP-36), #6 (V1434 Her), and #8 (V0357 Del) are classified as variable stars in SIMBAD. The moderate activity of source #7 (HAT-P-12) as described in Knutson, Howard & Isaacson (2010) might justify the photometric variability. All of them present standard magnitude variations under 0.07 mag in the i band. Sources #5 and #9 are the same object, named HAT-P-20. It has been detected in the i and z bands in near 140 images. The magnetic activity of the star (Sun et al. 2017) explains the observed magnitude variations.

Hence, our catalogue might be suitable for detecting variables. From the previous exercise, we obtain an average standard deviation of 0.2 mag using the five more scattered sources in Fig. 13 and 1 σ . We therefore combine the $S < -0.12$ cut with the magnitude standard

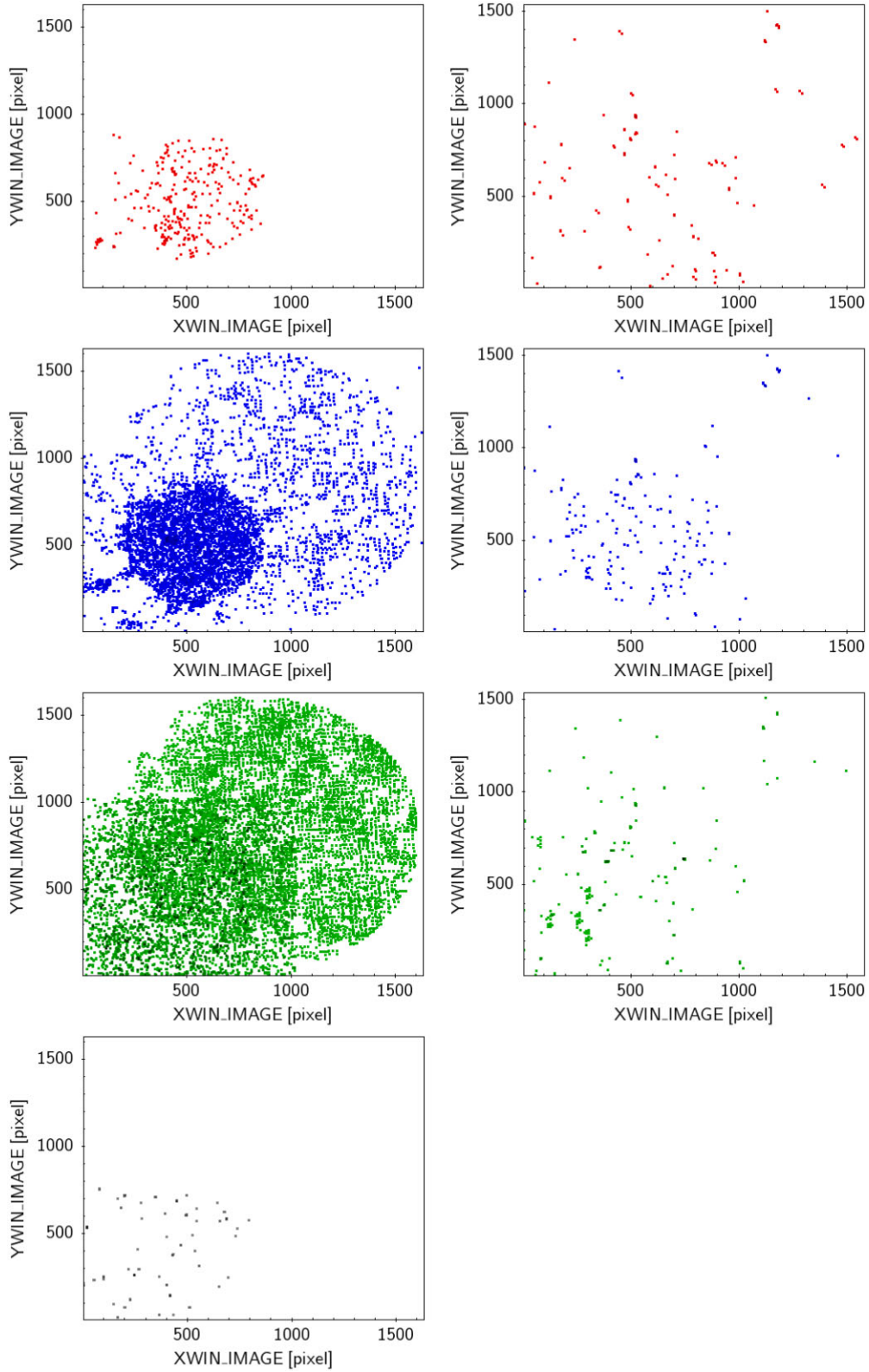


Figure 10. CCD xy position of sources with SDSS (left-hand panel) or APASS (right-hand panel) good-quality photometry and absolute differences larger than 0.27/0.09, 0.21/0.16, 0.18/0.12, and 0.14 magnitudes in g (red), r (blue), i (green), and z (grey) in SDSS/APASS, respectively.

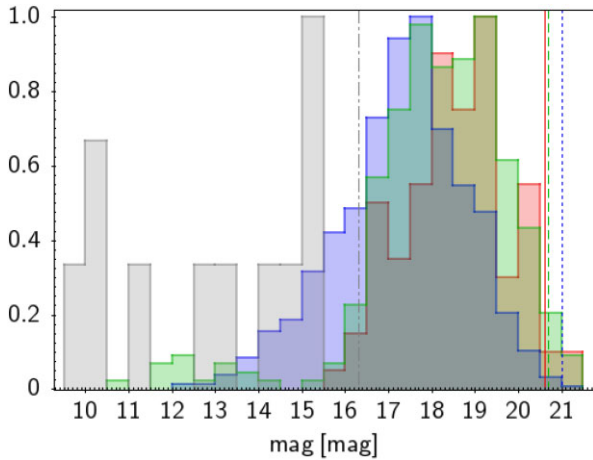


Figure 11. Normalized distributions of magnitudes of sources with $S < -0.12$ in the g (red), r (blue), i (green), and z (black) bands. Vertical coloured solid, dashed, and dot-dashed lines represent the magnitude detection limits in the catalogue for each filter with the same colour code.

deviation over 0.2 mag of sources detected more than five times in the same filter to identify variable candidates in our catalogue.

Out of the 2457 unique sources in each filter (note that there can be sources detected in more than one filter) with $S < -0.12$ and five or more detections, 28, 151, and 32 have a standard deviation of magnitudes larger than 0.2 mag in the g , r , and i bands, respectively. None in the z satisfies both criteria. Accounting for two targets that fulfill the criteria in more than one filter, there are a total of 209 different sources in the catalogue that are likely photometric variables. Keeping sources with $S < -0.12$ in more than one filter drastically reduces the chances of being photometric variations associated to atmospheric conditions or noise not covered by the photometric uncertainties. They are listed in a separate table in the archive (see Section 9 for details) and at CDS through the Vizier service. A more detailed study including a proper characterization of these sources is beyond the scope of this paper.

8 SCIENTIFIC EXPLOITATION

To illustrate the science capabilities of the CAFOS DR1 catalogue, we have defined the following three use cases.

8.1 Identification of asteroids

Solar System Objects (SSOs) such as asteroids are frequently found serendipitously crossing the field of view of astronomical observations. Their fast apparent motion due to their closeness makes challenging their identification. The *ssos* pipeline (Mahlke et al. 2019) has been developed to detect and identify SSOs based mainly on their linear apparent motion in subsequent exposures. The detection and association of the sources are performed with *SEXTRACTOR* and *SCAMP*, respectively. SSOs are distinguished from other sources in the images by performing a chain of user-configurable filter algorithms.

Before running the pipeline, we grouped the 6616 CAFOS images observed in SDSS filters by sky region and observation run. There are 155 groups with four or more exposures, which is the minimum required for obtaining a reliable detection of a SSO. A total of 6055 images are considered for the search.

The *ssos* pipeline identified 20 SSOs with 446 detections in 341 images, 13 of which are already known according to the IMCCE Virtual Observatory Solar System Portal’s SkyBoT service.⁹ This service computes the ephemerides of SSOs within a given field-of-view and observation epoch, which were cross-matched with the positions of the recovered SSOs in a 10 arcsec radius. The number and classification of previously known SSOs detected in our images are summarized in Table 3. The remaining seven SSOs are not known, having no registered asteroids with larger position uncertainties within 1 arcmin. Astrometry of the 446 detections has been reported to the Minor Planet Center.¹⁰ Their acceptance proves the goodness of the astrometry in the CAFOS catalogue. An example of an Apollo known asteroid identified in the images is shown in Fig. 14.

The low number of detections gathered and the short temporal baseline of each detected SSO prevents us from obtaining a spectrophotometric classification or a rotational period from the light-curve analysis. None the less, the combination of our observations with other data will help in the characterization of these asteroids.

8.2 Transient candidates

The resulting catalogue provides accurate astrometry and photometry for 139 337 detections in the optical *griz* bands. Among those detections, we identify 523 entries corresponding to 516 unique sources that have no counterpart in the *Gaia* EDR3, SDSS DR12, or Pan-STARRS DR1 (Kaiser et al. 2010; Chambers et al. 2016) optical surveys within 5 arcsec. All of them lie in the sky region covered by *Gaia* EDR3 and Pan-STARRS DR1 and all but 17 in the region covered by SDSS DR12. These surveys are deeper compared to CAFOS and all the 523 entries studied here are brighter than 21.3 mag, thus, being expected to have been detected in the aforementioned surveys. They represent the 0.4 per cent of the CAFOS photometric catalogue. Fig. 15 shows one of these sources observed in the g , r , and i filters, as an example.

The normalized distributions of the signal-to-noise ratio, ellipticity, FWHM, and `spread_model` of the 523 detections is shown in Fig. 16. The distributions of the whole catalogue are displayed as well for comparison. We can see how the histogram of the signal-to-noise ratio of the transient candidates shows two peaks, in contrast to the distribution of the catalogue, which presents only one. Out of the 523 detections, 212 (40 per cent of the sample) correspond to asteroids identified in the previous analysis with *ssos* and explain the second peak in the distribution (see the first panel in Fig. 16). An example of one of them is shown in Fig. 14.

Out of the remaining 304 sources (516–212), only one has an entry in the SIMBAD astronomical data base: GRB 190627A, classified as a gamma-ray burst (Fig. 15). We also found 22 counterparts in the Zwicky Transient Facility (ZTF; Bellm et al. 2018; Masci et al. 2018) archive, one in the *GALEX* GR6+7 AIS (Bianchi, Shiao & Thilker 2017) catalogue, 22 in UKIDSS LAS9 (Casali et al. 2007), DENIS (Epchtein et al. 1999; Fouqué et al. 2000) and/or ALLWISE (Cutri et al. 2021), and 184 counterparts in NEOWISE (Mainzer et al. 2011), all of them within 5 arcsec. All of these counterparts correspond to 198 sources. This is a remarkable result as it confirms the real nature of (at least, a significant fraction of) our transient candidates discarding other options like artefacts or spurious features that may have escaped from the quality control process.

⁹<http://vo.imcce.fr/webservices/skybot/>

¹⁰<https://www.minorplanetcenter.net/>

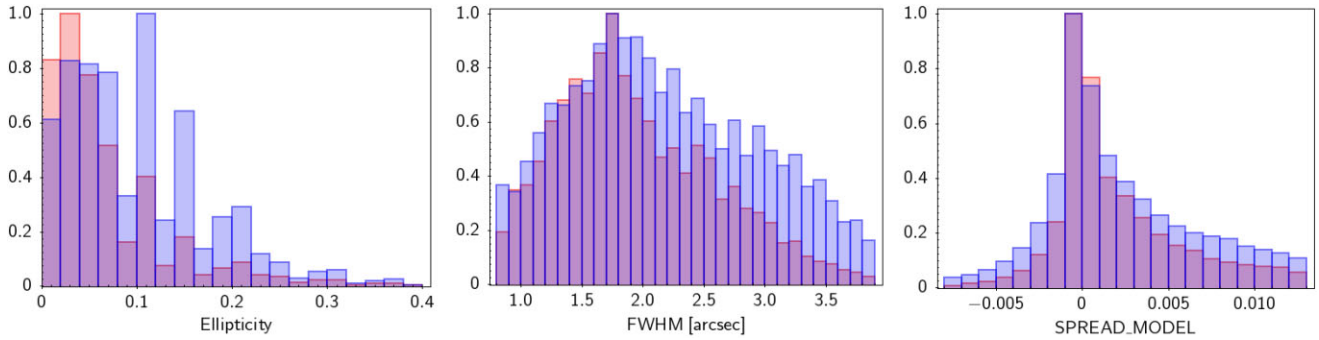


Figure 12. Normalized distributions of the ellipticity, FWHM, and SPREAD_MODEL from left to right of detections repeated more than five times in each filter with $S < -0.12$ mag (red) and with $S \geq -0.12$ mag (blue).

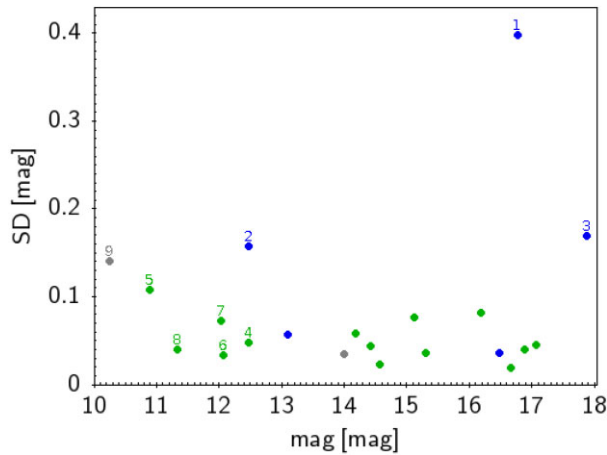


Figure 13. Standard deviation of magnitudes of known variable sources compared to their mean magnitudes. The blue, green, and grey filled circles stand for r , i , and z bands, respectively. Numbers refer to the nine sources with a standard deviation equal to or larger than the difference between the maximum and the minimum magnitude (or the amplitude), as provided in VSX. See the text for discussion.

Table 3. Classification of previously known SSOs detected in the DRI images. MB stands for Main-Belt. Number of detections in brackets.

Comet	Inner MB	Middle MB	Outer MB	Apollo
1 (63)	4 (123)	1 (12)	6 (61)	1 (144)

Sources with NEOWISE counterparts present $W1 - W2$ colours between -3.8 and 4.3 mag, regardless the photometric quality in the catalogue. The NEOWISE catalogue also provides the photometry of the associated ALLWISE source, which $W3$ band serves us to identify non-extragalactic sources by applying the relation $W1 - W2 > 0.96(W2 - W3) - 0.96$ derived by Kirkpatrick et al. (2011). There are 56 non-extragalactic sources in our sample with typical $W1 - W2$ colours of red and very red objects (from late K to late T/Y dwarfs and subdwarfs, e.g. fig. 1 in Kirkpatrick et al. 2011). This sources are properly identified in the catalogue.

We then attempt to characterize them by expanding the wavelength coverage using the photometric catalogues available from VOSA (Bayo et al. 2008), a Virtual Observatory tool to estimate physical parameters from the spectral energy distribution (SED) fitting to theoretical models. We gather photometry from GALEX-GR6+7, CAFOS, ZTF, DENIS, UKIDSS, WISE, and NEOWISE, and perform

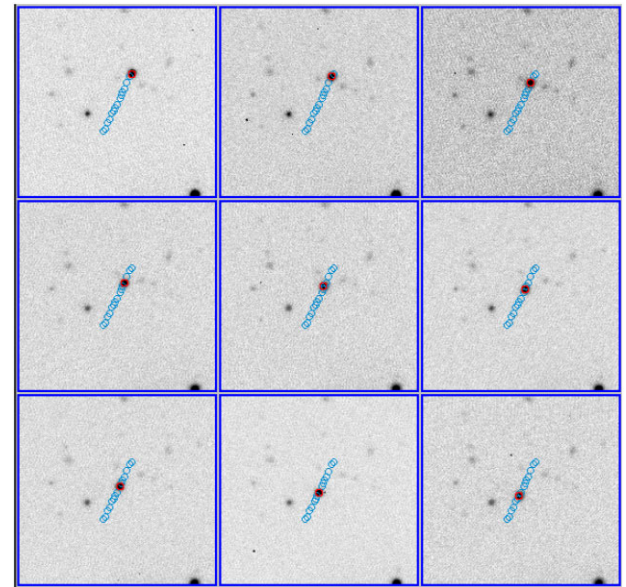


Figure 14. Example of linear motion of the Apollo asteroid Sisyphus during nine consecutive images centred at $RA = 12:39:49.3$ and $DEC = +52:13:52.0$. The temporal coverage of the full set is of near 46 min. The epoch increases from left to right and from top to bottom in intervals of 3.3 min as an average. The proper motion of the asteroid is $41.5'' h^{-1}$. The blue circles indicate the trajectory of the asteroid in a ~ 2.6 square arcmin sized field. The red circles indicate the current asteroid position in the image.

a χ^2 fit using the BT-Settl CIFIST grid of theoretical models (Husser et al. 2013; Baraffe et al. 2015) with $1200 < T_{\text{eff}} [\text{K}] < 7000$, $\log g = 4.5$ [dex] (sources were assumed to be dwarfs, although the impact of gravity on the model fitting is of second order), and solar metallicity. We obtain effective temperatures between 2400 and 4100 K for the six objects listed in Table 4. The internal uncertainty in the temperatures is 50 K, estimated as half the grid step of the model, although real temperature uncertainties are definitely larger since the maximum of the SED is poorly represented. Their corresponding SEDs are displayed in Fig. 17. These temperatures are compatible with a late-type K and five M solar metallicity dwarfs. All of them could thus be flaring objects that might have been observed with CAFOS during the flash events. Nevertheless, spectroscopic follow-up observations would be required for a proper characterization of these objects.

As a result, 105 (516–212–1–198) objects observed at different epochs and randomly distributed in the sky remain without further

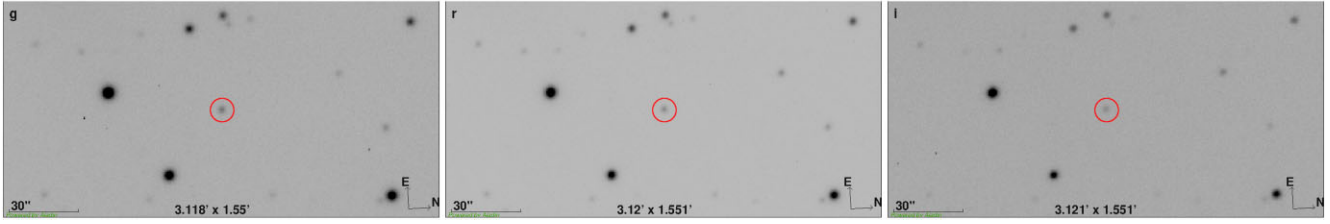


Figure 15. Example of a source (GRB 190627A, $i = 18.2$ mag), detected in the g , r , and i bands and with no counterpart in the *Gaia* EDR3, SDSS DR12, APASS DR9, or Pan-STARRS DR1 surveys.

information. Visual inspection reveals that near two-thirds are clearly confirmed as celestial bodies (over 60 targets). The remaining detections are more difficult to distinguish due to their low brightness. We identified some spurious detections close to bright sources or at the edge of the detector. Contamination in the sample of 523 detections without optical counterparts in public surveys is here estimated to be of 4 percent. They might be potential targets of interest, for instance, for studies on strong M-dwarf flares or on extreme stellar variability. The complete list of 523 detections will be accessible from the archive (see Section 9 for details) and at CDS through the VizieR service.

8.3 Identification of cool dwarfs

M dwarfs are the most common stars in the Milky Way (Kroupa 2001; Chabrier 2003). They are excellent tracers to study the structure, kinematics, and evolution of the Galaxy (e.g. Scalo 1986; Bochanski et al. 2007; Ferguson, Gardner & Yanny 2017). Also interesting is the fact that near one-third of M dwarfs are found in binary and multiple systems (e.g. Cortés-Contreras et al. 2017). Stellar companions located very close to the star are suitable for studying radii inflation (e.g. Cruz et al. 2018, 2022).

We identified and characterized cool dwarfs to validate CAFOS photometry. The r and i filters were adopted, since they have the greatest number of detections among all filters (see Table 1) and could provide information on the objects according to the colour ($r - i$), when both bands are available for the same object. Considering that only a small sample (over 3279 sources) have been observed with both filters, the selection was also based on *Gaia* photometry within 3 arcsec, where we adopted the colours ($G - r$) and ($i - G_{RP}$) to look for low temperature objects.

To select cool objects, we applied three different colour-cuts from the typical colours of M0V stars obtained in Cifuentes et al. (2020). Among the sources with available CAFOS r photometry, we kept those with available G magnitudes with relative errors of less than 10 percent. Then, we kept those sources with calculated $G - r$ colour of less than -0.17 mag – 3 142 objects. Similarly, among the sources with detections in the i -band and with good G_{RP} magnitude (within 10 percent error in *Gaia* magnitude), we selected the objects with ($i - G_{RP}$) > 0.36 mag – 2 941 objects. The last applied colour-cut considered all sources observed with both r and i filters. Among them, 584 objects presented ($r - i$) greater than 0.74 mag. We then, selected a total of 5719 different sources which respected at least one of the above applied colour-cuts and that are therefore photometric candidates to M-type or later dwarfs. It is worth mentioning that 456 of the selected objects follow the three criteria.

These M-star candidates underwent a second criterion, based on their effective temperatures. The T_{eff} were estimated from SED fitting obtained with VOSA. CAFOS r and i photometry were used to construct the SED – also g and z band CAFOS magnitudes when

available. We also searched for additional photometry available in the VO archives, covering the visible and infrared wavelengths, which are: SDSS DR12, *Gaia* eDR3, PanSTARRS DR2 (Flewelling et al. 2020, and references therein), 2MASS, IRAS, AKARI/IRC (Ishihara et al. 2010), and *WISE*. For the fit, we adopted the BT-Settl CIFIST models, with T_{eff} ranging from 1 200 to 7 000 K, $\log g$ from 2.5 to 5.5 dex, and solar metallicity ($[\text{Fe}/\text{H}] = 0.0$). Any IR photometric data that seemed as an excess – VOSA considers the photometric points which are above the best-fitting model by over 3σ to be an excess – were excluded from the fit. From the list of candidates, 4822 objects presented very good SED fits – based on the visual goodness of fit, V_{gfb} ¹¹ parameter estimated by VOSA of less than 8. We have then found 2322 objects with T_{eff} of less than 4000 K, corresponding to M stars or later spectral types. The histogram of obtained temperatures is presented in blue in Fig. 18. A cross-match with the Washington Double Star (WDS) catalogue (Mason et al. 2001) and the Exoplanet Encyclopaedia¹² indicates there are no counterparts in such catalogues. However, we found 58 M dwarfs in our sample with the *Gaia* RUWE parameter above 1.4, which suggest a bad astrometric solution that may be ascribed to the presence of a close companion (Arenou et al. 2018; Lindegren et al. 2018). One of them is an ultra cool dwarf of 1800 K.

The remaining objects with good SED fitting (4822–2322) presented higher temperatures, consistent with K-type stars. We attributed this to: (i) the initial selection was based on just one of the three applied colour-cuts; and (ii) the ($i - G_{RP}$) colour is more effective on discriminating ultracool objects, with stellar types later than M6, rather than earlier types (see table A.2 from Cifuentes et al. 2020, for more details).

In order to find a subset of nearby M dwarfs, we selected those that presented good parallax measurements (with a parallax relative error of less than 10 per cent) and with calculated distances inferior to 500 pc finding 395 objects. These stars are represented in a colour–magnitude diagram (CMD; Fig. 19) by different colours, showing the obtained effective temperature. Those objects with good parallaxes, but with calculated distances beyond 500 pc, are presented in black – 601 stars. As reference, we included in the CMD a sample of *Gaia* EDR3 sources with relative errors lower than 10 per cent in parallax and proper motion, shown in grey. The obtained T_{eff} for these nearby objects are illustrated in Fig. 18 in red.

Among our set of low-temperature objects, we identified 20 ultracool dwarfs – that is, M7 type or later, with temperatures ranging from 1500 to 2700 K, with associated types from M7 to L7. Three of them are included in the SIMBAD data base, two of which are identified as an M8 dwarf and a brown dwarf candidate. Both of them lie within 500 pc (91.4 and 102.8 pc, respectively). The remaining

¹¹For details, see VOSA help page.

¹²www.exoplanet.eu

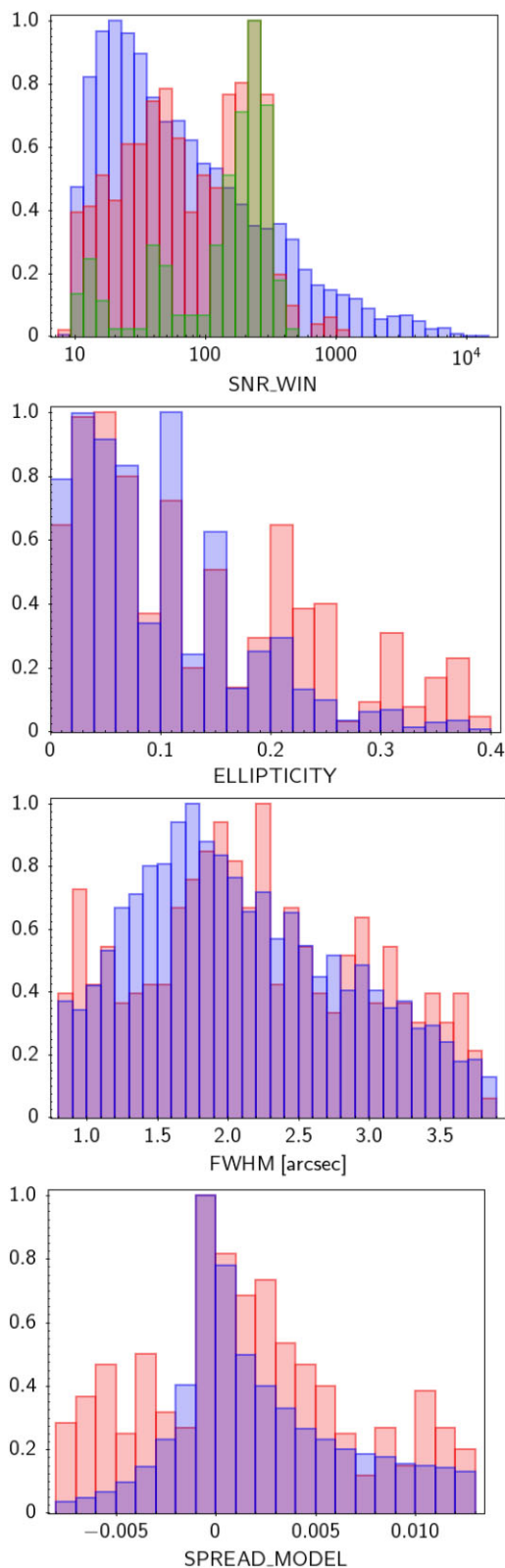


Figure 16. Normalized distributions of the signal-to-noise ratio, ellipticity, FWHM, and SPREAD_MODEL from left to right of the 523 detections with no counterpart in optical surveys (red) and in the whole catalogue (blue). Green on the first panel stands for the SSOs in the sample.

candidates require spectroscopic confirmation. The list of ultracool dwarf candidates is shown in Table 5 together with their measured CAFOS magnitudes in the i band (or r when i is not available). The complete list of 2322 low mass stars candidates will be available in the archive (see Section 9 for details), together with the sample of candidates at less than 500 pc and those that satisfy the three colour criteria. They will also be accessible through the CDS VizieR service.

9 DATA ACCESS

The astrometrically corrected CAFOS images are available from the CALAR ALTO Archive Portal¹³ as well as from the corresponding SIAP service¹⁴ while the catalogue can be accessed from an archive system¹⁵ or through a Virtual Observatory ConeSearch.¹⁶

This archive system provides a very simple search interface that allows queries by position or magnitude interval (Fig. 20). It also implements a link to the reduced images in the CALAR Alto archive. After launching the query, the result is presented in HTML format with all the detections that satisfy the search criteria. The output can also be downloaded as a VOTable or CSV file. The results can also be easily transferred to other VO applications like TOPCAT (Taylor 2005) through the SAMP protocol. Detailed information on the output fields can be obtained placing the mouse over the question mark (?) located near the name of the column.

10 CONCLUSIONS AND FUTURE WORK

In this work, we presented the first data release of the Calar Alto CAFOS direct imaging data, which includes on one hand, 42 173 ready-to-use processed and astrometrically calibrated images from 2008 March to 2019 July. On the other hand, it provides the photometric catalogue associated to 6132 images observed in Sloan’s $griz$ filters. It contains 139 337 point-like detections corresponding to 21 985 different sources taken between 2012 September and 2019 June. Exposure times in the catalogue range from 0.5 to 600 s.

We developed the CAFOS Photometry Calibrator (CFC) with the goal of automatically extracting the sources from the images, carrying out the selection of valid non-saturated sources and performing the flux calibration with the SDSS DR12 or APASS DR9 surveys as reference.

The final catalogue of point sources has a mean internal astrometric accuracy of 0.05 arcsec. The mean internal photometric accuracy is 0.04 mag and the averaged standard deviation of magnitudes of sources detected more than five times in each filter is of 0.08 mag. No dependence on colour, binning mode, or pixel position was found. Additionally, we conducted an exercise to assess the presence of real variable objects in the catalogue and obtained a sample of 209 targets suitable for a variability analysis.

To demonstrate the science capabilities of the photometric catalogue, we explore three different science cases. We first searched for SSOs that serendipitously cross the FoV of the images. We recovered 446 positions in 341 images of 20 SSOs, seven of which are unknown. These results have been shared with the Minor Planet Center. Secondly, we inspected a sample of 516 sources without counterparts in the *Gaia* EDR3, SDSS DR12, or Pan-STARRS

¹³<https://caha.sdc.cab.inta-csic.es/calto/jsp/searchform.jsp>

¹⁴http://caha.sdc.cab.inta-csic.es/calto/siap/caha_siap.jsp?

¹⁵<http://svocats.cab.inta-csic.es/caha-cafos/>

¹⁶e.g. <http://svocats.cab.inta-csic.es/caha-cafos-detection/cs.php?RA=356.979&DEC=32.346&SR=0.1&VERB=2>

Table 4. Targets of interest characterized with VOSA.

Detection ID	RA (hms)	DEC (dms)	T_{eff} (K)
CAHA_CAFOS_BBI_DR1_168496_0262	01:51:12.13	+ 10:46:33.4	2 500
CAHA_CAFOS_BBI_DR1_168493_0123	01:51:37.11	+ 10:50:14.4	2 500
CAHA_CAFOS_BBI_DR1_168563_0030	01:51:51.73	+ 10:40:20.5	2 800
CAHA_CAFOS_BBI_DR1_168566_0134	07:58:17.13	+ 52:41:39.3	3 600
CAHA_CAFOS_BBI_DR1_137808_0087	12:15:41.78	+ 02:07:49.2	2 400
CAHA_CAFOS_BBI_DR1_121051_0064	23:12:59.21	+ 11:07:53.8	4 100

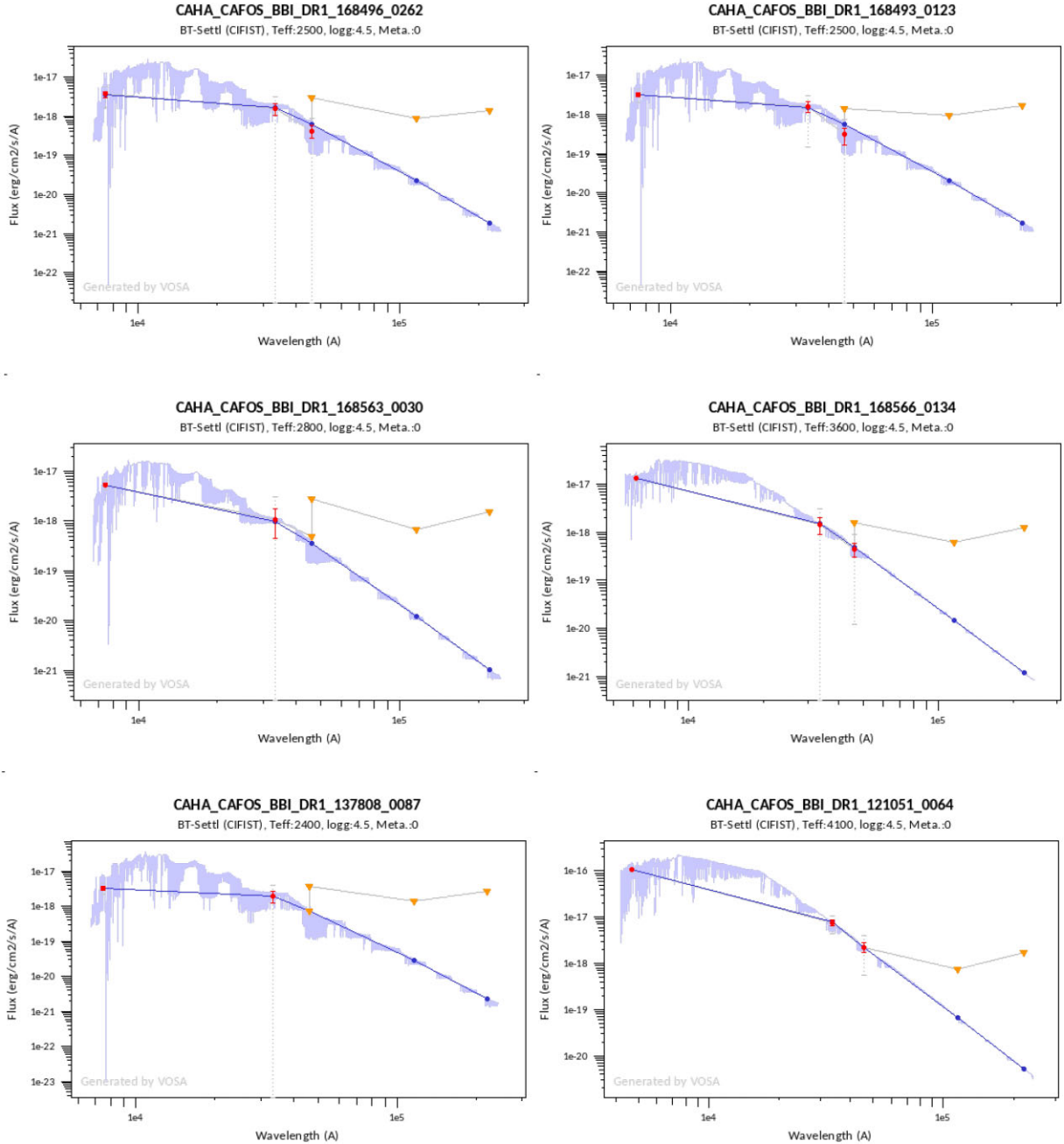


Figure 17. Spectral energy distributions of the six low mass stars identified with VOSA with no optical counterpart. The blue spectrum represents the theoretical model that best fits and red circles represent the observed photometry used for the fit. The inverted yellow triangles indicate that the photometric values correspond to upper limits, which generally come from the W2 band in *WISE* or *NEOWISE*, and W3 and W4 *WISE* bands.

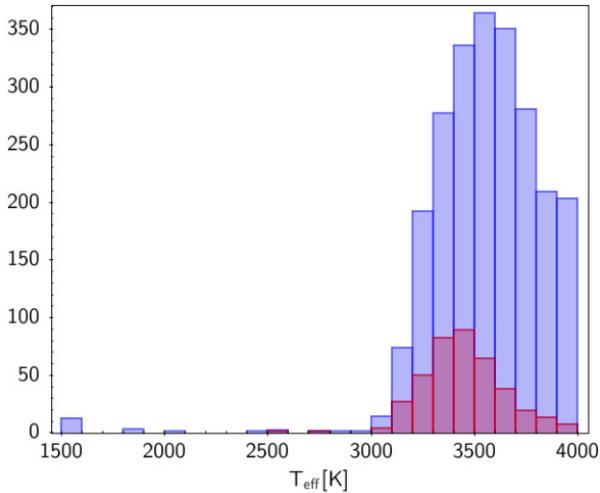


Figure 18. Histogram of effective temperatures obtained from SED fitting with VOSA. The T_{eff} for the M-star sample (with 2322 objects) are presented in blue. The identified nearby cool dwarfs (within 500 pc) are shown in red.

DR1 optical surveys. One of them is a known gamma-ray burst, another 22 have counterparts in the ZTF archive, and near 40 per cent (203 objects) have NEOWISE photometry, meaning there are very red objects in the sample. For six targets, we complemented our optical magnitudes with infrared photometry and provided effective temperatures between 2400 and 4100 K from their SED analysis using VOSA. These are estimated K–M dwarfs that might happen to flare during the observations. Furthermore, near 40 per cent are related to moving SSOs recovered previously with the *ssos* pipeline. Around 60 targets lack of further information for a proper characterization and are proposed as potential targets of interest for studies on M dwarf flares or stellar variability, for instance. At last, we looked for cool dwarfs in the catalogue from the application of three colour cuts in the optical wavelength range using photometry in the r and i bands together with *Gaia*'s. We identified 2322 sources

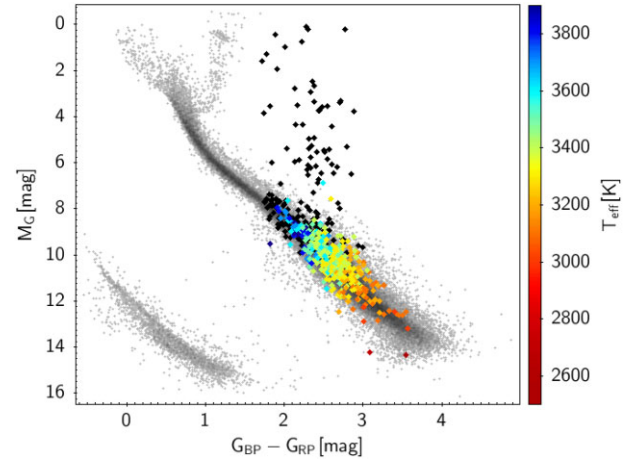


Figure 19. Colour–magnitude diagram of identified M stars with good parallax measurements from *Gaia* EDR3. Nearby cool stars within 500 pc are presented colour coded, according to their estimated temperatures. More distant objects, but with good parallaxes, are presented in black. A sample of *Gaia* EDR3 sources with good parallax and proper motions are shown in grey.

with effective temperatures ranging between 1500 and 3900 K obtained with VOSA, 326 of which satisfy the three colour criteria simultaneously. 58 M dwarfs have a *Gaia*'s RUWE parameter over 1.4, which is related to a bad astrometric solution possibly ascribed to the presence of a close companion. Out of the 2322 low mass stars candidates, 20 are ultra cool dwarfs that present temperatures under 2700 K. Additionally, we defined a subset of 395 nearby cool dwarfs with distances closer than 500 pc.

For new releases of the catalogue we aim at including rejected images in this work and images observed in filters different than the Sloan's *griz* bands. Also new public broad-band images that will be delivered over the life of the instrument would be included. In order to improve the photometric quality of the catalogue, we plan to test the photometric calibration by using the ATLAS All-Sky Stellar Ref-

Table 5. Ultracool dwarf candidates identified in the catalogue.

Source NID	RA (hms)	DEC (dms)	T_{eff} (K)	i_mag (mag)
21884 ^a	01:28:50.58	+ 21:03:09.4	2700	20.77 ^c
7491 ^b	12:33:05.35	+ 44:55:34.9	2500	18.38
11850	18:40:34.62	−00:02:26.5	1500	15.24
16673	18:40:38.25	−00:01:08.2	1800	17.96
11928	18:40:40.21	+ 00:01:12.0	1500	16.32
11991	18:40:45.46	+ 00:03:26.1	1500	17.53
12003	18:40:46.35	+ 00:04:53.7	1800	17.94
12042	18:40:49.94	+ 00:05:06.8	1500	16.86
16660	18:40:51.37	+ 00:03:36.6	2500	18.11
12079	18:40:53.19	+ 00:02:55.5	1500	16.84
12101	18:40:54.58	+ 00:00:31.6	1500	13.98
12120	18:40:56.34	+ 00:04:05.5	1800	17.21
12129	18:40:56.90	+ 00:04:19.6	1500	17.07
12147	18:40:58.56	+ 00:01:53.3	1500	15.63
12161	18:41:00.01	+ 00:00:44.5	2400	14.49
12190	18:41:02.78	+ 00:01:20.4	1500	17.00
12193	18:41:02.85	−00:01:57.3	1500	16.73
12198	18:41:03.26	+ 00:03:01.5	1500	17.03
12232	18:41:06.58	−00:01:21.6	1500	16.75
16577	18:42:58.56	+ 00:27:36.3	2050	14.89 ^c

Note. ^a Brown dwarf candidate (Reylé 2018). ^b Classified as M8V (West et al. 2011). ^c Magnitudes in the r filter.

SVO Calar Alto CAFOS Direct Imaging First Data Release archive

Detection catalogue.

Figure 20. Screenshot of the archive search interface that permits simple queries to the detection catalogue.

erence Catalog (Tonry et al. 2018) as well as *Gaia* spectra from which we could derive photometry without requiring further corrections.

Given the heterogeneity of the observing conditions and purposes of the images, and despite the homogeneous treatment applied in this work, the complete absence of errors and problems in the catalogue cannot be guaranteed. Users are therefore encouraged in these cases to download and check the images to assess the reliability of a given catalogue measurement. The *News* section of the catalogue website will contain a list of Frequently Asked Questions as well as a description of caveats that may arise with the scientific exploitation of the catalogue.

ACKNOWLEDGEMENTS

This research is part of the project I+D+i with reference PID2020-112949GB-I00, supported by the MCIN/AEI/10.13039/501100011033 and MDM-2017-0737 at Centro de Astrobiología (CSIC-INTA), Unidad de Excelencia María de Maeztu, and the ESCAPE project supported by the European Commission Framework Programme Horizon 2020 Research and Innovation action under grant agreement n. 824064. NC acknowledges financial support from the Spanish Programa Estatal de I+D+i Orientada a los Retos de la Sociedad under grant RTI2018-096188-B-I00, which is partly funded by the European Regional Development Fund (ERDF). PC acknowledges financial support from the Government of Comunidad Autónoma de Madrid (Spain), via postdoctoral grant ‘Atracción de Talento Investigador’ 2019-T2/TIC-14760. MCC thanks Max Mahlke for his valuable support in the *ssos* usage. This research has made use of the Spanish Virtual Observatory (<http://svo.cab.inta-csic.es>) supported from Ministerio de Ciencia e Innovación (MCIN) through grant PID2020-112949GB-I00. This publication makes use of VOSA, developed under the Spanish Virtual Observatory project supported by the Spanish Ministerio de economía y competitividad (MINECO) through grant AyA2017-84089. VOSA has been partially updated by using funding from the European Union’s Horizon 2020 Research and Innovation Programme, under Grant Agreement no 776403 (EXOPLANETS-A). This research has made use of the SVO Filter Profile Service (<http://svo2.cab.inta-csic.es/theory/fps/>) supported from the Spanish MINECO through grant AYA2017-84089. This research has made use of SVOCAT developed by the Spanish Virtual Observatory project funded by MCIN/AEI/10.13039/501100011033/ through

grant PID2020-112949GB-I00. This research has made use of the cross-match service, the SIMBAD data base (Wenger et al. 2000), VizieR catalogue access tool (Ochsenbein, Bauer & Marcout 2000), ‘Aladin sky atlas’ (Bonnarel et al. 2000; Boch & Fernique 2014) provided by Centre de Données astronomiques de Strasbourg (CDS), Strasbourg, France. This research has also made use of the TOPCAT (Taylor 2005) and STILTS (Taylor 2006). This research has made use of IMCCE’s SkyBoT VO tool (Berthier et al. 2006), *ssos* (Mahlke et al. 2019), SEXTRACTOR (Bertin & Arnouts 1996), PSFEX (Bertin 2011), SCAMP (Bertin 2006). This research has made use of the NASA/IPAC Infrared Science Archive, which is funded by the National Aeronautics and Space Administration and operated by the California Institute of Technology. This research has made use of the International Variable Star Index (VSX) data base, operated at AAVSO, Cambridge, Massachusetts, USA. This research was made possible through the use of the AAVSO Photometric All-Sky Survey (APASS), funded by the Robert Martin Ayers Sciences Fund and NSF AST-1412587. This work has made use of data from the European Space Agency (ESA) mission *Gaia* (<https://www.cosmos.esa.int/gaia>), processed by the *Gaia* Data Processing and Analysis Consortium (DPAC, <https://www.cosmos.esa.int/web/gaia/dpac/consortium>). Funding for the DPAC has been provided by national institutions, in particular the institutions participating in the *Gaia* Multilateral Agreement. This work has been possible thanks to the extensive use of IPython and Jupyter notebooks (Pérez & Granger 2007), as well as the Python packages ASTROPY,¹⁷ a community-developed core Python package for Astronomy (The Astropy Collaboration 2013; Price-Whelan et al. 2018), ASTROQUERY (Ginsburg et al. 2019), NUMPY (Harris et al. 2020), SCIPY (Virtanen et al. 2020), and MATPLOTLIB (Hunter 2007).

DATA AVAILABILITY

The data underlying this article are available in the SVO Calar Alto CAFOS Direct Imaging First Data Release archive at <http://svocats.cab.inta-csic.es/caha-cafos/>.

¹⁷<http://www.astropy.org>

REFERENCES

- Alam S. et al., 2015, *ApJS*, 219, 12
- Arenou F. et al., 2018, *A&A*, 616, A17
- Baraffe I., Homeier D., Allard F., Chabrier G., 2015, *A&A*, 577, A42
- Bayo A., Rodrigo C., Barrado Y Navascués D., Solano E., Gutiérrez R., Morales-Calderón M., Allard F., 2008, *A&A*, 492, 277
- Bellm E. C. et al., 2018, *PASP*, 131, 018002
- Berthier J., Vachier F., Thuillot W., Fernique P., Ochsenbein F., Genova F., Lainey V., Arlot J. E., 2006, in Gabriel C., Arviset C., Ponz D., Enrique S., eds, ASP Conf. Ser. Vol. 351, *Astronomical Data Analysis Software and Systems XV*. Astron. Soc. Pac., San Francisco, p. 367
- Bertin E., 2006, in Gabriel C., Arviset C., Ponz D., Enrique S., eds, ASP Conf. Ser. Vol. 351, *Astronomical Data Analysis Software and Systems XV*. Astron. Soc. Pac., San Francisco, p. 112
- Bertin E., 2011, in Evans I. N., Accomazzi A., Mink D. J., Rots A. H., eds, ASP Conf. Ser. Vol. 442, *Astronomical Data Analysis Software and Systems XX*. Astron. Soc. Pac., San Francisco, p. 435
- Bertin E., 2013, PSFEx: Point Spread Function Extractor, *Astrophysics Source Code Library*, record ascl:1301.001
- Bertin E., Arnouts S., 1996, *A&AS*, 117, 393
- Bianchi L., Shiao B., Thilker D., 2017, *ApJS*, 230, 24
- Boch T., Fernique P., 2014, in Manset N., Forshay P., eds, ASP Conf. Ser. Vol. 485, *Astronomical Data Analysis Software and Systems XXIII*. Astron. Soc. Pac., San Francisco, p. 277
- Bochanski J. J., Munn J. A., Hawley S. L., West A. A., Covey K. R., Schneider D. P., 2007, *AJ*, 134, 2418
- Bonnarel F. et al., 2000, *A&AS*, 143, 33
- Cardiel N. et al., 2020, in XIV.0 Scientific Meeting (virtual) of the Spanish Astronomical Society. p. 219
- Casali M. et al., 2007, *A&A*, 467, 777
- Chabrier G., 2003, *PASP*, 115, 763
- Chambers K. C. et al., 2016, preprint ([arXiv:1612.05560](https://arxiv.org/abs/1612.05560))
- Cifuentes C. et al., 2020, *A&A*, 642, A115
- Cortés-Contreras M. et al., 2017, *A&A*, 597, A47
- Cortés-Contreras M., Bouy H., Solano E., Mahlke M., Jiménez-Esteban F., Alacid J. M., Rodrigo C., 2020, *MNRAS*, 491, 129
- Cruz P., Diaz M., Birkby J., Barrado D., Sipőcz B., Hodgkin S., 2018, *MNRAS*, 476, 5253
- Cruz P., Aguilar J. F., Garrido H. E., Diaz M. P., Solano E., 2022, *MNRAS*, 515, 1416
- Cutri R. M. et al., 2021, *VizieR Online Data Catalog*, p. II/328
- Epchtein N. et al., 1999, *A&A*, 349, 236
- Ferguson D., Gardner S., Yanny B., 2017, *ApJ*, 843, 141
- Flewelling H. A. et al., 2020, *ApJS*, 251, 7
- Fouqué P. et al., 2000, *A&AS*, 141, 313
- Gaia Collaboration, 2016, *A&A*, 595, A1
- Gaia Collaboration, 2018, *A&A*, 616, A1
- Ginsburg A. et al., 2019, *AJ*, 157, 98
- Harris C. R. et al., 2020, *Nature*, 585, 357
- Henden A. A., Levine S., Terrell D., Welch D. L., 2015, *American Astronomical Society Meeting Abstracts #225*, 336.16
- Hunter J. D., 2007, *Comput. Sci. Eng.*, 9, 90
- Husser T. O., Wende-von Berg S., Dreizler S., Homeier D., Reiners A., Barman T., Hauschildt P. H., 2013, *A&A*, 553, A6
- Ishihara D. et al., 2010, *A&A*, 514, A1
- Kaiser N. et al., 2010, in Stepp L. M., Gilmozzi R., Hall H. J. eds, *Proc. SPIE Conf. Ser. Vol. 7733, Ground-based and Airborne Telescopes III*. SPIE, Bellingham, p. 159
- Kirkpatrick J. D. et al., 2011, *ApJS*, 197, 19
- Knutson H. A., Howard A. W., Isaacson H., 2010, *ApJ*, 720, 1569
- Kroupa P., 2001, *MNRAS*, 322, 231
- Lawrence A. et al., 2007, *MNRAS*, 379, 1599
- Lindegren L. et al., 2018, *A&A*, 616, A2
- Mahlke M., Solano E., Bouy H., Carry B., Verdoes Kleijn G., Bertin E., 2019, *Astron. Comput.*, 28, 100289
- Mainzer A. et al., 2011, *ApJ*, 731, 53
- Masci F. J. et al., 2018, *PASP*, 131, 018003
- Mason B. D., Wycoff G. L., Hartkopf W. I., Douglass G. G., Worley C. E., 2001, *AJ*, 122, 3466
- Ochsenbein F., Bauer P., Marcout J., 2000, *A&AS*, 143, 23
- Pérez F., Granger B. E., 2007, *Comput. Sci. Eng.*, 9, 21
- Reylé C., 2018, *A&A*, 619, L8
- Price-Whelan A. M. et al., 2018, *AJ*, 156, 123
- Scalo J. M., 1986, *Fund. Cosmic Phys.*, 11, 1
- Skrutskie M. F. et al., 2006, *AJ*, 131, 1163
- Sun L. et al., 2017, *AJ*, 153, 28
- Taylor M. B., 2005, in Shopbell P., Britton M., Ebert R., eds, ASP Conf. Ser. Vol. 347, *Astronomical Data Analysis Software and Systems XIV*. Astron. Soc. Pac., San Francisco, p. 29
- Taylor M. B., 2006, in Gabriel C., Arviset C., Ponz D., Enrique S., eds, ASP Conf. Ser. Vol. 351, *Astronomical Data Analysis Software and Systems XV*. Astron. Soc. Pac., San Francisco, p. 666
- The Astropy Collaboration, 2013, *A&A*, 558, A33
- Tony J. L. et al., 2018, *ApJ*, 867, 105
- Virtanen P. et al., 2020, *Nat. Methods*, 17, 261
- Watson C. L., Henden A. A., Price A., 2006, *Soc. Astron. Sci. Ann. Symp.*, 25, 47
- Wenger M. et al., 2000, *A&AS*, 143, 9
- West A. A. et al., 2011, *AJ*, 141, 97
- Wright E. L. et al., 2010, *AJ*, 140, 1868
- York D. G. et al., 2000, *AJ*, 120, 1579

APPENDIX A: CONFIGURATION FILES

Table A1. Configuration parameters for the first iteration of SEXTRACTOR.

Catalog	
CATALOG_NAME ^a	CFC_configuration/sextractor_result_files/test_psf.cat
CATALOG_TYPE ^b	FITS_LDAC
PARAMETERS_NAME	CFC_configuration/sextractor_configuration_files/prepsfex.param
Extraction	
DETECT_TYPE	CCD
DETECT_MINAREA	12
DETECT_MAXAREA	0
THRESH_TYPE	RELATIVE
DETECT_THRESH	1.5
ANALYSIS_THRESH	1.5
FILTER	Y
FILTER_NAME	CFC_configuration/sextractor_configuration_files/gauss_2.5_5x5.conv
DEBLEND_NTHRESH	32
DEBLEND_MINCONT	0.005
CLEAN	Y
CLEAN_PARAM	1.0
MASK_TYPE	CORRECT
Photometry	
PHOT_APERTURES	20,25,30
PHOT_AUTOPARAMS	2.5, 3.5
PHOT_PETROPARAMS	1.0,3.5
PHOT_AUTOAPERS	0.0,0.0
PHOT_FLUXFRAC	
SATUR_LEVEL	50000.0
SATUR_KEY	DUMMY
MAG_ZEROPOINT	0.0
MAG_GAMMA	4.0
GAIN	0.0
GAIN_KEY	GAIN
PIXEL_SCALE	0
Star/Galaxy Separation	
SEEING_FWHM ^c	1.2
STARNNW_NAME	CFC_configuration/sextractor_configuration_files/default.nnw
Background	
BACK_SIZE	64
BACK_FILTERSIZE	5
BACKPHOTO_TYPE	GLOBAL
Check Image	
CHECKIMAGE_TYPE ^d	NONE
CHECKIMAGE_NAME ^e	check.fits,aper.fits
Memory	
MEMORY_OBJSTACK	30000
MEMORY_PIXSTACK	300000
MEMORY_BUFSIZE	1800
Miscellaneous	
WEIGHT_TYPE	NONE
VERBOSE_TYPE	NORMAL
HEADER_SUFFIX ^f	.head
INTERP_MAXLAG ^f	16
INTERP_MAXYLAG ^f	16
INTERP_TYPE ^f	NONE
PSF_NAME ^f	CFC_configuration/sextractor_result_files/test_psf.psf
PATTERN_TYPE ^f	RINGS-HARMONIC
SOM_NAME ^f	default.som

^a Notes. Catalogue name was renamed to 'test.cat' for the second iteration of SEXTRACTOR.

^b Catalogue type was changed to 'ASCII_HEAD' for the second iteration of SEXTRACTOR.

^c Stellar seeing was modified to 2.5 for the second iteration of SEXTRACTOR.

^d Checkimage type was modified to 'BACKGROUND' for the second iteration of SEXTRACTOR.

^e Checkimage name was modified to 'CFC_configuration/sextractor_result_files/bkg.fits'.

^f Only included in the configuration file of the second iteration of SEXTRACTOR.

Table A2. Configuration parameters for PSFEx.

PSF model	
BASIS_TYPE	PIXEL_AUTO
BASIS_NUMBER	20
BASIS_NAME	basis.fits
BASIS_SCALE	1.0
NEWBASIS_TYPE	NONE
NEWBASIS_NUMBER	8
PSF_SAMPLING	0.0
PSF_PIXELSIZE	1.0
PSF_ACCURACY	0.01
PSF_SIZE	31,31
PSF_RECENTER	Y
MEF_TYPE	INDEPENDENT
Point source measurements	
CENTER_KEYS	X_IMAGE,Y_IMAGE
PHOTFLUX_KEY	FLUX_APER(1)
PHOTFLUXERR_KEY	FLUXERR_APER(1)
PSF variability	
PSFVAR_KEYS	X_IMAGE,Y_IMAGE
PSFVAR_GROUPS	1,1
PSFVAR_DEGREES	3
PSFVAR_NSAP	9
HIDDENMEF_TYPE	COMMON
STABILITY_TYPE	EXPOSURE
Sample selection	
SAMPLE_AUTOSELECT	Y
SAMPLEVAR_TYPE	SEEING
SAMPLE_FWHMRANGE	1.0,15.0
SAMPLE_VARIABILITY	0.05
SAMPLE_MINSN	20
SAMPLE_MAXELLIP	0.3
SAMPLE_FLAGMASK	0x00fe
SAMPLE_WFLAGMASK	0x00ff
SAMPLE_IMAFLAGMASK	0x0
BADPIXEL_FILTER	N
BADPIXEL_NMAX	0
PSF homogenization kernel	
HOMOBASIS_TYPE	NONE
HOMOBASIS_NUMBER	10
HOMOBASIS_SCALE	1.0
HOMOPSF_PARAMS	2.0, 3.0
HOMOKERNEL_DIR	
HOMOKERNEL_SUFFIX	.homo.fits
Output catalogs	
OUTCAT_TYPE	NONE
OUTCAT_NAME	CFC_configuration/sextractor_result_files/psfex_out.cat
Check-plots	
CHECKPLOT_DEV	NULL
CHECKPLOT_RES	0
CHECKPLOT_ANTIALIAS	Y
CHECKPLOT_TYPE	NONE
CHECKPLOT_NAME	NONE
Check-Images	
CHECKIMAGE_TYPE	NONE
CHECKIMAGE_NAME	chi.fits,proto.fits,samp.fits,resi.fits,snap.fits
CHECKIMAGE_CUBE_N	
Miscellaneous	
PSF_DIR	
PSF_SUFFIX	.psf
VERBOSE_TYPE	NORMAL
WRITE_XML	N
XML_NAME	psfex.xml
XSL_URL	file:///usr/share/psfex/psfex.xsl
NTHREADS	1

Downloaded from https://academic.oup.com/mnras/article/521/2/3127/707556 by Universidad Complutense Madrid user on 13 April 2020

Table A3. Parameters obtained from SEXTRACTOR and PSFEX.

NUMBER	Running object number	
ALPHA_J2000	Right ascension of barycenter (J2000)	(deg)
DELTA_J2000	Declination of barycenter (J2000)	(deg)
X_IMAGE	Object position along x	(pixel)
Y_IMAGE	Object position along y	(pixel)
A_IMAGE	Profile RMS along major axis	(pixel)
B_IMAGE	Profile RMS along minor axis	(pixel)
THETA_IMAGE	Position angle (CCW/x)	(deg)
XWIN_IMAGE	Windowed position estimate along x	(pixel)
YWIN_IMAGE	Windowed position estimate along y	(pixel)
XMIN_IMAGE	Minimum x-coordinate among detected pixels	(pixel)
YMIN_IMAGE	Minimum y-coordinate among detected pixels	(pixel)
XMAX_IMAGE	Maximum x-coordinate among detected pixels	(pixel)
YMAX_IMAGE	Maximum y-coordinate among detected pixels	(pixel)
X_WORLD	Barycenter position along world x axis	(deg)
Y_WORLD	Barycenter position along world y axis	(deg)
ERRX2_WORLD	Variance of position along X-WORLD (alpha)	(deg**2)
ERRY2_WORLD	Variance of position along Y-WORLD (delta)	(deg**2)
FLAGS	Extraction flags	-
FLAGS_WEIGHT	Weighted extraction flags	-
FWHM_IMAGE	FWHM assuming a gaussian core	(pixel)
FWHM_WORLD	FWHM assuming a gaussian core	(deg)
FLUX_MAX	Peak flux above background	(count)
FLUX_RADIUS	Fraction-of-light radii	(pixel)
FLUX_PSF	Flux from PSF-fitting	(count)
FLUXERR_PSF	RMS flux error for PSF-fitting	(count)
MAG_PSF	Magnitude from PSF-fitting	(mag)
MAGERR_PSF	RMS magnitude error from PSF-fitting	(mag)
FLUX_AUTO	Flux within a Kron-like elliptical aperture	(count)
FLUXERR_AUTO	RMS error for AUTO flux	(count)
MAG_AUTO	Kron-like elliptical aperture magnitude	(mag)
MAGERR_AUTO	RMS error for AUTO magnitude	(mag)
ELONGATION	A_IMAGE/B_IMAGE where A_IMAGE is the profile RMS along the major axis and B_IMAGE is the profile RMS along the minor axis	-
ELLIPTICITY	1 - B_IMAGE/A_IMAGE (where A_IMAGE is the profile RMS along the major axis and B_IMAGE is the profile RMS along the minor axis)	-
SNR_WIN	Signal-to-noise ratio in a Gaussian window	-
SPREAD_MODEL	Spread parameter from model-fitting	-

APPENDIX B: CATALOGUE DESCRIPTION

Table B1. Description of the parameters contained in the source catalogue.

Parameter	Units	Description
SourceNID	–	Numerical ID of sources detected more than once within 0.5 arcsec
RAJ2000	deg	Celestial Right Ascension (J2000)
DEJ2000	deg	Celestial Declination (J2000)
e_RAJ2000	arcsec	Right ascension error
e_DEJ2000	arcsec	Declination error
Detection_ID	–	Detection identifier
Image_identifier	–	Image identifier
Image_url	–	URL to access the reduced image
gmag	mag	PSF calibrated magnitude in the <i>g</i> band
e_gmag	mag	PSF calibrated magnitude error in the <i>g</i> band
rmag	mag	PSF calibrated magnitude in the <i>r</i> band
e_rmag	mag	PSF calibrated magnitude error in the <i>r</i> band
imag	mag	PSF calibrated magnitude in the <i>i</i> band
e_imag	mag	PSF calibrated magnitude error in the <i>i</i> band
zmag	mag	PSF calibrated magnitude in the <i>z</i> band
e_zmag	mag	PSF calibrated magnitude error in the <i>z</i> band
Flag_phot	–	Calibration flag. ‘A’ stands for calibrated magnitudes within the interval of magnitudes used for the photometric calibration, ‘B’ for calibrated magnitudes fainter than the faintest magnitudes, and ‘C’ for calibrated magnitudes brighter magnitudes than the brightest magnitude used for the photometric calibration.
Filter	–	Filter of observation
Refcat	–	Reference catalogue used for the photometric calibration
Elongation	–	Elongation of the detection
Ellipticity	–	Ellipticity of the detection
FWHM	arcsec	Full width half maximum of the detection
SNR_WIN	–	Signal to noise ratio
SPREAD_MODEL	–	Spread parameter from model-fitting. It takes values close to zero for point sources, positive for extended sources (galaxies), and negative for detections smaller than the PSF, such as cosmic ray hits.
MJD	d	Modified Julian Date
DATE-OBS	iso-8601	Observing epoch
SourceSize	–	Number of detections for each source in GroupID

This paper has been typeset from a $\text{\TeX}/\text{\LaTeX}$ file prepared by the author.